A generic computational model for three-dimensional fracture and fragmentation problems of quasi-brittle materials

Liwei Guo[a,1,*], Jiansheng Xiang[a], John-Paul Latham[a] and Bassam Izzuddin[b]

[a] *Department of Earth Science and Engineering, Imperial College London, South Kensington Campus, London SW7 2AZ, United Kingdom*

[b] *Department of Civil and Environmental Engineering, Imperial College London, South Kensington Campus, London SW7 2AZ, United Kingdom*

E-mail address: liwei.guo@ucl.ac.uk (Liwei Guo)
j.xiang@imperial.ac.uk (Jiansheng Xiang)
j.p.latham@imperial.ac.uk (John-Paul Latham)
b.izzuddin@imperial.ac.uk (Bassam Izzuddin)

Declarations of interest: none

Abstract

Fracture and fragmentation in three dimensions are of great importance to understand the mechanical behaviour of quasi-brittle materials in failure stress states. In this paper, a generic computational model has been developed in an in-house C/C++ code using the combined finite-discrete element method, which is capable of modelling the entire three-dimensional fracturing process, including pre-peak hardening deformation, post-peak strain softening,

* Corresponding author.

[1] Present address: Department of Mechanical Engineering, University College London, Torrington Place, London WC1E 7JE, United Kingdom.

transition from continuum to discontinuum, and explicit interaction between discrete fragments. The computational model is validated by Brazilian tests and polyaxial compression tests, and a realistic multi-layer rock model in an *in situ* stress condition is presented as an application example. The results show that the computational model can capture both continuum and discontinuum behaviour and therefore it provides an ideal numerical tool for fracture and fragmentation problems.
Keywords: computational model, finite element method, discrete element method, fracture, fragmentation, 3D, quasi-brittle material, Mohr-Coulomb criterion

1 Introduction

The mechanical behaviour of quasi-brittle materials, such as rock, concrete and ceramics, is frequently concerned with fracture and fragmentation when they reach their strengths under failure conditions. In the analyses of these problems, although several special geometries and loading conditions can be simplified into two-dimensional problems, when complex geometry and loading conditions are considered, three-dimensional analysis tools are essential to accurately characterise the stress field and material failure in realistic scenarios. With the prolific development of computer technology in recent decades, an increasing amount of research has been devoted to the development of numerical codes for the understanding of fracture and fragmentation problems of practical interest. However, three-dimensional fracture and fragmentation simulations still pose a major challenge in terms of modelling both continuum and discontinuum behaviour in complex three-dimensional stress fields.

One group of methods traditionally used in this area is the finite element method (FEM) and the extended finite element method (XFEM). Original FEM methods are mainly applied for modelling continuum media. By introducing material damage models into the FEM formulations, however, they are capable of modelling strong discontinuities, e.g. fractures. Underpinning many popular FEM implementations of fracture models is the theory that inelastic deformation in solids is usually accompanied by the formation of localised bands of

intense straining, i.e. strain localisation. Once strain localisation happens, large strains can accumulate inside a narrow band and eventually lead to fracture (Ortiz et al., 1987; Oliver, 1996; François and Keita, 2015; Tvergaard, 2015). Originated from the traditional FEM methods, the XFEM method is based on the partition of unity method that enriches the FEM shape functions to capture the discontinuities in materials (Belytschko and Black, 1999; Malekan et al, 2018; Jansari et al., 2019). The main advantages of FEM-based fracture models are their high accuracy compared with analytical solutions because the FEM formulation is very versatile in terms of accommodating the implementations of different theoretical models. However, the majority of FEM-based fracture models can only simulate the fracturing process up and until fracture formation, whereas the stage after that when discrete fracture surfaces interact with each other, e.g. frictional sliding, and interaction between fragments generated in multi-body collision problems, are often outside the scope of these models.

By contrast, another group of methods, also widely used for fracture modelling, originates from the simulation of discontinuous media, e.g. granular materials. One typical method in this category is the discrete element method (DEM), which solves the equations of motion of discrete bodies. Each discrete body in the DEM domain is considered as a unique free body that can interact when it makes contact with its surrounding bodies, so contact detection and interaction are two important aspects in the DEM formulation. Due to the intrinsic characteristic of the DEM method to be able to simulate discrete bounded bodies in contact and separated by discontinuities, various fracture modelling approaches have been developed based on the DEM formulation (Cundall and Strack, 1979; Shi and Goodman, 1985; Martin et al., 2003; Morris et al., 2004; Calvetti, 2008; Baraldi et al., 2015; Radi et al., 2019). These methods normally discretise the domain as a granular system of discrete bodies (blocks or particles) and fractures are explicitly represented by the debonding of elements. The main advantage is that actual materials can be represented by assembling discrete particles (e.g. bonded together to represent rock or unboned for soil), the mechanical behaviour at the macroscale can be captured as an emergent property of the assembly using simpler assumptions and fewer parameters at the microscale (Cundall, 2001).

For example, the DEM has been extensively used in the field of failure modelling of granular soils. Darve et al. (2004) analysed grain avalanches, where local failures are characterised by bursts of kinetic energy; similar simulations of such diffuse failure modes were also conducted by others (Nicot et al., 2007; Sibille et al., 2007; Sibille et al., 2008; Nicot et al., 2011). Delenne et al. (2004) simulated compression tests on large samples of a cohesive granular material. Li et al. (2005) developed a new discrete particle model in the framework of dynamics model for failure modelling of granular materials. Lobo-Guerrero and Vallejo (2005) modelled granular materials in direct shear tests, where particle breakage is realised by replacing one particle with multiple particles of different sizes. Peron et al. (2009) included cohesive forces between grains in the DEM formulation to simulate drying shrinkage and cracking of fine-grained soils. Yan et al. (2010) developed ellipsoidal DEM to represent more realistic particle shapes in granular media and a multiscale modelling methodology for the contact with solid deformable bodies. Wang and Yan (2013) simulated granular soils and showed the shear failure modes varied as a function of particle breakage. Obermayr et al. (2013) developed a bonded-particle model for cemented sand and obtained realistic macroscopic behaviour in triaxial compression tests. Ciantia et al. (2016) used a crushing model (Ciantia et al., 2015) to simulate incremental responses of granular soils, in which grain crushing contributes to the incremental irreversible strain. Cil et al. (2020) proposed a three-dimensional DEM model to reproduce the size-dependent particle strength in brittle granular materials using a bonded particle framework.

One problem with pure DEM is the characterisation of complex shaped bodies, i.e. complex boundary geometry, and complicated internal stress fields are not as accurate as the FEM-based models. Therefore, a new strategy in the numerical modelling of fracture and fragmentation problems is to combine different methods so that the limitations of each individual method can be reduced or overcome by other methods to achieve synergy. For example, the combination of the FEM formulation and the DEM formulation can simulate both continuum behaviour, e.g. the accurate calculation of strain and stress, and the discontinuum behaviour caused by fracturing and multi-body contact, e.g. the interaction across discontinuities, which is not possible to achieve in either single formulation.

In the category of combined FEM and DEM formulations, different research groups have proposed various strategies. For example, Oñate and Rojek (2004) combined the DEM for granular soil/rock materials and the FEM for other parts in the system. Monteiro Azevedo and Lemos (2006) proposed a hybrid method that uses the DEM in the discretisation of the fracture zone and the FEM for the surrounding area. Morris et al. (2006) discretised the discrete blocks internally with tetrahedral elements and implemented Cosserat point theory and cohesive elements to simulate fractures. Kh. et al. (2008, 2011) developed a two-dimensional model to simulate breakage of angular particles in granular systems, where particles are simulated by the DEM, and after each step of DEM analysis every particle is individually modelled by the FEM to determine if it will break. Paavilainen et al. (2009) used the nonlinear Timoshenko beam element and the cohesive crack model for the FEM part, whereas the contact forces between colliding beams are calculated by the DEM. Elmekati and El Shamy (2010) combined the DEM for near-structure zone and the FEM for far-field that is not affected by the structure. Ma et al. (2016) used breakable cohesive interface elements in the FEM discretisation of individual particles and concluded granular soils may reach a steady state under high compressive stresses or shear strains (Ma et al., 2019). Tu et al. (2017) developed a separate edge coupling method to capture the soil failure process by modelling the local granular behaviour and reducing the computational cost in the remaining domain. Gui et al., (2018) simulated a field soil desiccation test using a hybrid continuum-discrete element method, which can model multiple fractures and grain deformation. Nadimi and Fonseca (2018) modelled grain-to-grain interactions in a combined framework so as to link grain scale parameters with the macroscale response of soils.

Particularly, many combined FEM and DEM models for granular materials use a two-scale strategy to integrate both the macroscale (continuum) and the microscale (particle) into one framework. Kaneko et al. (2003) developed a two-scale model based on the homogenisation theory, using the DEM at the microscale and the FEM at the macroscale. Miehe et al. (2010) proposed a two-scale discrete-to-finite element model, where a homogenised standard continuum is considered at the coarse scale and the granular microstructures, represented by aggregates of particles, are attached to each material point.

Andrade et al. (2011) proposed a model to simulate complex behaviour of granular materials by extracting key continuum properties directly from the grain-scale mechanics. Li et al. (2014) developed a mixed FEM procedure of the gradient Cosserat continuum, without the need to specify the macroscopic properties, such as the constitutive relationship and the failure model. Nguyen et al. (2014) used DEM simulations to calculate the average stress and the consistent tangent operators at each macroscopic integration point. Guo and Zhao (2016a, 2016b) presented a multiscale modelling approach, in which DEM assemblies are attached to the Gauss points in the FEM mesh to derive the required constitutive relations for granular soils (Zhao and Guo, 2015).

The computational model introduced in this paper has been developed using one of the combined methods, which is called the combined finite-discrete element method (FEMDEM). In the FEMDEM simulations, the entire domain is treated as a multi-body system and each discrete element is further discretized into a mesh of finite elements. Therefore, discontinuum behaviour is analysed by the DEM while the continuum behaviour is analysed by the FEM. Here the discontinuum behaviour means multi-body interactions and contacts at discontinuous interfaces, e.g. fracture surfaces. The continuum behaviour means the deformation and stress may vary from place to place inside the discrete elements, i.e. on finite element meshes. The FEMDEM method has been widely applied in a variety of engineering problems (Xiang et al., 2009; Mahabadi et al., 2012; Guo et al., 2015). However, the three-dimensional FEMDEM codes that have been reported for almost as long have not until recently included a fracture model for specific scenarios (Klerck et al., 2004; Rougier et al., 2014).

The objective of this paper is to develop a generic computational model for simulations of three-dimensional discrete tensile and shear fracture initiation and propagation for quasi-brittle materials. The novelty of this model is that it combines both the finite element method (FEM) and the discrete element method (DEM) with smooth transition. More specifically, the intact material before fracture initiation is modelled as a continuum domain using the FEM formulation. After fracture initiation the domain is mixed with continua and fractures, where the FEM formulation remains in the continua whereas the contact algorithms in the DEM

formulation is switched on for the interaction between discrete fracture surfaces. A Mohr-Coulomb criterion with a tension cut-off is used to determine the shear strength based on the normal stress acting perpendicular to the shear direction in complex stress fields. Moreover, the DEM formulation enables the computational model to use its advantage of dealing with large displacement problems.

In this paper, first the formulations of the computational model are introduced. The new algorithms, such as the space discretisation scheme and the transition from continuum to discontinuum are described in detail. Next, three numerical examples are presented, including Brazilian tests, polyaxial compression tests and the simulation of a realistic three-dimensional multi-layer rock model in an *in situ* stress condition. The first two tests are chosen to validate the capability of the computational model to simulate both tensile and shear fractures. In the third example, the three-dimensional multi-layer rock model is created from a fracture pattern map and simulated to investigate stress heterogeneity and fracture pattern formation in a realistic geological setting. Last, the numerical results are discussed, and some conclusions are drawn from this work.

2 Computational model

From a physical point of view, a fracture model should characterise the stress state for fracture initiation and the orientation and speed for fracture propagation. In order to simulate this transition from continuum to discontinuum numerically, the computational model developed in this paper uses both the finite element method (FEM) and the discrete element method (DEM). The novelty of this new development is that the two formulations are used in separate time domains and space domains and are linked by smooth transition. More specifically, in the time domain, the FEM formulation is used before fracture formation and after material failure the DEM formulation is activated; in the space domain, the deformation and stresses in the continuum are calculated by the FEM formulation and the interaction forces between physically discrete fracture surfaces are calculated by the contact algorithms

in the DEM formulation. The overall algorithm for three-dimensional fracturing simulations is shown in Figure 1.

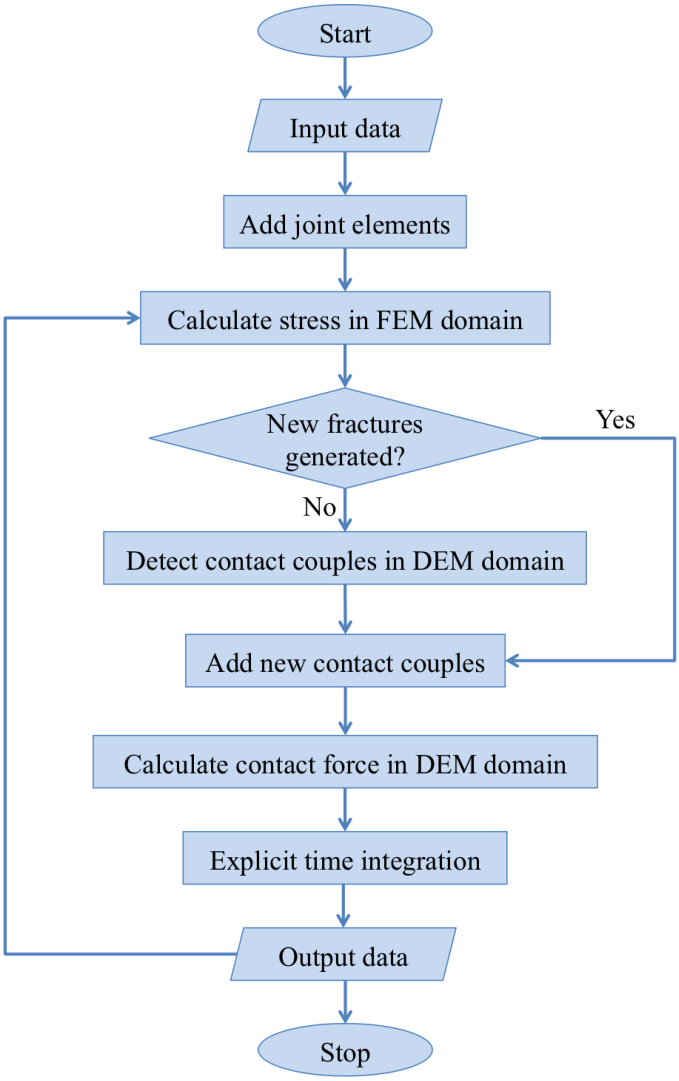

Figure 1: Flowchart of three-dimensional fracturing simulations.

2.1 Space discretisation and joint element

The computational model works in a domain discretised by 4-node tetrahedral elements and special 6-node joint elements. In order to simulate the fracturing process explicitly, the tetrahedral elements are allowed to separate according to a failure criterion so that fracture surfaces can be represented by the faces of tetrahedral elements. There are two main advantages of physically separating tetrahedral elements. First, the interaction between fracture surfaces (Salehani et al., 2019), e.g. stick-slip frictional events, can be captured

realistically by modelling the contact between separated tetrahedral elements (Guo et al., 2017). Second, other media, such as fluids, can be introduced between discrete fracture surfaces for coupling simulations. To achieve the objective of separating tetrahedral elements, 6-node joint elements are inserted between 4-node tetrahedral elements (Figure 2) so the failure criterion can be applied to the joint elements.

2.2 Stress calculation and failure criterion

Deformation in three-dimensional domain generates stresses both in the 4-node tetrahedral elements and 6-node joint elements. The fracture model in this paper is similar to the concept proposed by Hillerborg et al. (1976), which assumes that the material is softened but still continuous by the constraint of bonding stresses σ_b in the plastic zone ahead of the real fracture. The bonding stress σ_b inside the plastic zone decreases from material strength σ_s at the end of the plastic zone to zero at the real fracture tip. In reality, the plastic zone corresponds to a micro-fractured region with some remaining ligaments for stress transfer (Meng et al., 2019). In this paper, the Hillerborg model is extended into three dimensions and considers bonding stresses both in the normal and shear directions. The shear strength is dependent on the normal stress by the Mohr-Coulomb criterion. The formation and propagation of discreet fractures are implemented by breaking joint elements and subsequently separating tetrahedral elements.

The Cauchy stress tensor **T** in tetrahedral elements is calculated by a neo-Hookean viscoelastic constitutive model (Bonet and Wood, 1997),

$$\mathbf{T} = \frac{\mu}{J}(\mathbf{B} - \mathbf{I}) + \frac{\lambda}{J}(\ln J)\mathbf{I} + \eta\mathbf{D} \tag{1}$$

where μ and λ are Lamé constants; **B** is the Left Cauchy-Green strain tensor; J is the determinant of the deformation gradient matrix **F**; η is the viscous damping parameter; and **D** is the rate of deformation, which is calculated from the symmetric velocity gradient **L** (Munjiza, 2004).

$$\mathbf{D} = \frac{1}{2}(\mathbf{L} + \mathbf{L}^{\mathrm{T}}) \tag{2}$$

The stresses in joint elements are calculated from the relative displacements between adjacent tetrahedral elements. In Figure 2 the deformation in joint element $N_1N_2N_3$-$N_4N_5N_6$ is characterised by the displacement between the two triangular faces $N_1N_2N_3$ and $N_4N_5N_6$. The displacement vector $\boldsymbol{\delta}$ of a joint element is defined as

$$\boldsymbol{\delta} = (\delta_n, \delta_s)^{\mathrm{T}} \tag{3}$$

where δ_n is the normal displacement; and δ_s is the shear displacement. Each joint element has three integration points, such as A, B and C for joint element $N_1N_2N_3$-$N_4N_5N_6$ in Figure 2. The displacement vector $\boldsymbol{\delta}$ is calculated at each integration point in a local coordinate system $x'y'z'$; the $x'y'$-plane passes through three points N_{16}, N_{25} and N_{34}, which are midpoints between N_1 and N_6, N_2 and N_5, and N_3 and N_4, respectively. The normal displacement δ_n is defined in the z'-direction, and the shear displacement δ_s is defined in the $x'y'$-plane, which has two components in the x' and y' directions, respectively.

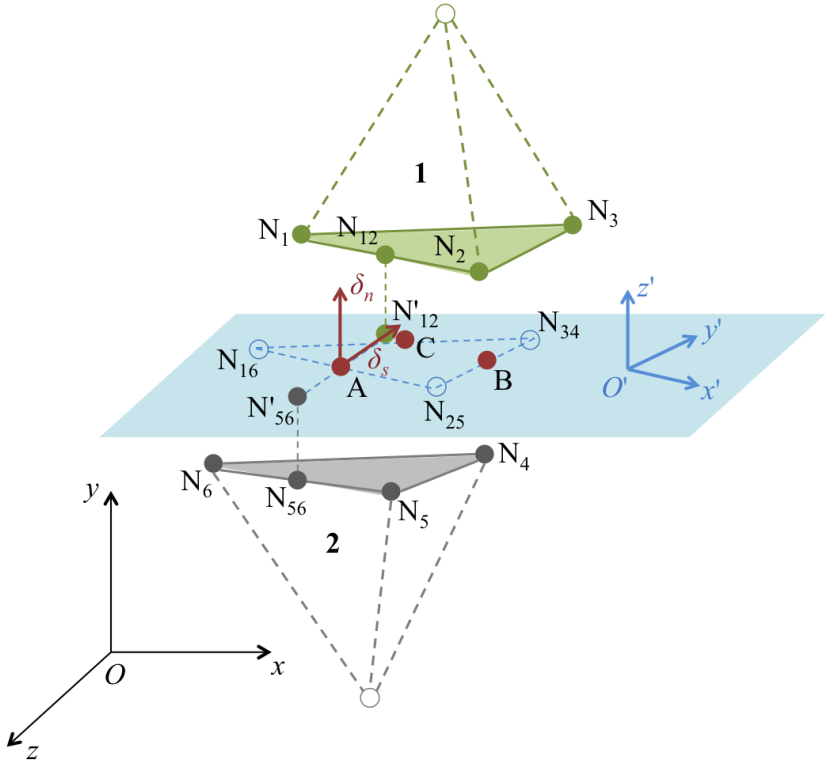

Figure 2: Local coordinate system of a joint element. N_{16}, N_{25} and N_{34} are midpoints between N_1 and N_6, N_2 and N_5, and N_3 and N_4, respectively. A, B and C are integration points of this joint element $N_1N_2N_3$-$N_4N_5N_6$. N_{12} and N_{56} are midpoints between N_1 and N_2, and N_5 and N_6, respectively.

Correspondingly, the stress vector $\boldsymbol{\sigma}$ in a joint element is defined in the normal and shear directions as

$$\boldsymbol{\sigma} = (\sigma, \tau)^{\mathrm{T}} \tag{4}$$

where σ is the normal stress, corresponding to the normal displacement δ_n; and τ is the shear stress, corresponding to the shear displacement δ_s. It should be noted that the term *stress vector* is specially used for the joint elements because the three-dimensional stress tensor is reduced to only two components, so the term *vector* is used. The stress vector in joint elements is calculated based on a stress-displacement relation (Figure 3) similar to the combined single and smeared crack model proposed by Munjiza et al. (1999). The normal stress σ and shear stress τ are calculated following different values of parameters on the curve.

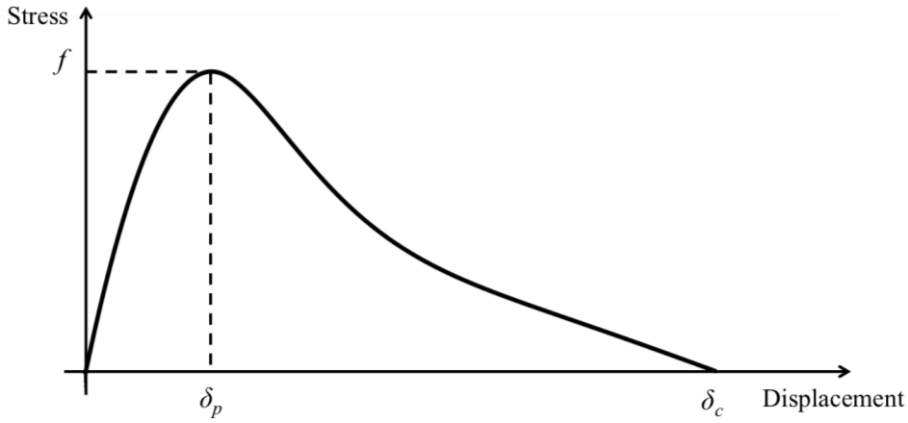

Figure 3: The stress-displacement relation for joint elements.

The peak stress f represents the material strength, which means the tensile strength f_t for the normal stress σ_n and the shear strength f_s for the shear stress τ. The tensile strength f_t is assumed to be a constant, whereas the shear strength f_s is determined by the Mohr-Coulomb criterion with a tension cut-off,

$$f_s = c - \sigma_n \tan\phi \tag{5}$$

where c is the cohesion; ϕ is the internal friction angle; σ_n is the normal stress acting perpendicular to the shear direction. It should be noted that because the normal stress σ_n cannot exceed the tensile strength f_t, the tension cut-off that happens when $\sigma_n \geq f_t$ is automatically guaranteed in Equation 5.

δ_p is the maximum hardening displacement corresponding to the peak stress f. In the normal direction and shear directions, δ_{np} and δ_{sp} can be calculated as follows,

$$\delta_{np} = 2\frac{f_t}{p_0}h \tag{6}$$

$$\delta_{sp} = 2\frac{f_s}{p_0}h \tag{7}$$

where f_t is the tensile strength; f_s is the shear strength defined in Equation 5; h is the mean length of the edges of the joint element; p_0 is the penalty term characterising the stiffness of the joint element so in the limit,

$$\lim_{p_0 \to \infty} \delta_p = 0 \tag{8}$$

In numerical simulations, ideally the value of the penalty term p_0 should be large enough so that the extra elasticity introduced into the domain by the joint elements can be negligible (Klein et al., 2001; Turon et al., 2007). However, a larger penalty term may cause numerical stability problems (Schellekens and de Borst, 1993), which usually requires smaller time-steps in the explicit time integration scheme. For the current serial numerical code, the computational time would be unbearably long if the time-step is too small. Therefore, to maintain a balance between accuracy and computational efficiency, the value of the penalty term p_0 is usually chosen as

$$E \leq p_0 \leq 10E \tag{9}$$

where E is the Young's modulus assigned for the tetrahedral elements.

In Figure 3, δ_c is the critical displacement at which the joint element fails. The definition of δ_c is based on the Griffith theory (Griffith, 1921), which assumes that a certain amount of energy is absorbed by the formation of a unit area of the fracture surface in a brittle medium. This absorbed energy is defined as the fracture energy G_f, which can be calculated as

$$G_f = \int_{\delta_p}^{\delta_c} \sigma d\delta \approx \frac{1}{3} f \delta_c \tag{10}$$

Equation 10 can be used for both tensile and shear fractures but with different values, e.g. G_{ft} and G_{fs}. It should be noted that in Equation 10 the area under a parabola is used as an approximation to calculate the area under the exponential curve.

Next, the normal stress σ can be calculated from the normal displacement δ_n by Equation 11, similar to the concept of calculating forces in an assembly of discrete particles connected by springs.

$$\sigma = \begin{cases} 2\dfrac{\delta_n}{\delta_{np}} f_t, & \text{if } \delta_n < 0 \\ \left[2\dfrac{\delta_n}{\delta_{np}} - \left(\dfrac{\delta_n}{\delta_{np}}\right)^2\right] f_t, & \text{if } 0 \le \delta_n \le \delta_{np} \\ z f_t, & \text{if } \delta_{np} \le \delta_n \le \delta_{nc} \end{cases} \tag{11}$$

where δ_{np} is the maximum hardening displacement in the normal direction (Equation 6); δ_{nc} is the critical displacement at failure in the normal direction (Equation 10); z is a heuristic softening parameter by curve fitting using experiment data (Xian et al., 1991; Munjiza et al., 1999),

$$z = \left[1 - \frac{a+b-1}{a+b}\exp\left(D\frac{a+bc}{(a+b)(1-a-b)}\right)\right][a(1-D) + b(1-D)^c] \tag{12}$$

where a = 0.63, b = 1.8 and c = 6.0 are material properties derived from experiment data. Although they were derived originally for concrete, the same values are adopted in this paper to represent typical quasi-brittle materials due to the lack of specific experimental data and the large overlap of material properties between different quasi-brittle materials. D is a parameter calculated considering both the normal displacement δ_n and the shear displacement δ_s,

$$D = \begin{cases} \dfrac{\delta_n - \delta_{np}}{\delta_{nc} - \delta_{np}}, & \text{if } \delta_{np} < \delta_n < \delta_{nc} \text{ and } \delta_s < \delta_{sp} \\ \dfrac{\delta_s - \delta_{sp}}{\delta_{sc} - \delta_{sp}}, & \text{if } \delta_{sp} < \delta_s < \delta_{sc} \text{ and } \delta_n < \delta_{np} \\ \sqrt{\left(\dfrac{\delta_n - \delta_{np}}{\delta_{nc} - \delta_{np}}\right)^2 + \left(\dfrac{\delta_s - \delta_{sp}}{\delta_{sc} - \delta_{sp}}\right)^2}, & \text{if } \delta_{np} < \delta_n < \delta_{nc} \text{ and } \delta_{sp} < \delta_s < \delta_{sc} \\ 1, & \text{if } \delta_n \ge \delta_{nc} \text{ or } \delta_s \ge \delta_{sc} \\ 0, & \text{Otherwise} \end{cases} \tag{13}$$

where δ_{sp} is the maximum hardening displacement in the shear direction (Equation 7); δ_{sc} is the critical displacement at failure in the shear direction (Equation 10). In a similar way, the shear stress τ can be calculated by substituting the normal displacement δ_n with the shear displacement δ_s, and other parameters in the normal direction (with subscript n) with the corresponding parameters in the shear direction (with subscript s) in Equation 11.

The stresses in joint elements change non-linearly along the edges of joint elements. A numerical integration scheme derived by Hammer et al. (1956) is used to calculate the nodal forces $\mathbf{f}_{joint}$ contributed by the stresses in joint elements. The stresses at the three integration points of a joint element (Figure 2) are checked to determine if that joint element fails. A joint element is labelled as failed when at least two integration points have zero stress components. The failure of a joint element causes physical separation of the two adjacent tetrahedral elements, so a discrete fracture will be formed. It should be noted that the computational model proposed in this paper is based on a fixed mesh, so fractures can only initiate and propagate along faces of tetrahedral elements.

2.3 Transition from continuum to discontinuum

The transition from continuum to discontinuum in the computational model can be explained from two perspectives: from a physical point of view, the original continuum domain (intact without fractures) becomes a domain mixed with strong discontinuities caused by fracturing; from a numerical point of view, the tetrahedral elements originally connected by joint elements are physically separated and the interaction between them is simulated by the contact algorithms in the DEM formulation, including contact detection and contact interaction. Because the entire domain is discretised by tetrahedral elements and joint elements, the contact means contact between tetrahedral elements. The contact detection algorithm finds couples of tetrahedral elements that are in contact, and the contact interaction algorithm calculates the forces between the tetrahedral elements. The contact detection is a key factor for the computational efficiency, and the contact interaction is important to achieve a smooth transition from continuum to discontinuum.

The contact detection algorithm is called *no binary search* (NBS) algorithm (Munjiza and Andrews, 1998; Munjiza, 2004), which has two functions: collision between discrete bodies, and normal and tangential separation between discrete fracture surfaces (Tvergaard, 2003). To improve the computational efficiency, instead of finding contact couples everywhere in the domain, the contact detection in the continuum region (no fractures) is only activated after new factures are formed. More specifically, after fracture formation, new contact couples,

which are pairs of tetrahedral elements at both sides of the new fracture, should be added to the contact couple list. This procedure is described as follows. First, a contact couple C_{ff} of the two tetrahedral elements tet^+ and tet^- at both sides of the failed joint element is added to the contact couple list,

$$C_{ff} = \{tet^+, tet^-\} \tag{14}$$

Next, the other neighbouring tetrahedral elements of the failed joint element are selected to form six groups of tetrahedral elements as $G_1 \sim G_6$ because each joint element has six nodes. For example, the group G_1 is defined as,

$$G_1 = \{tet_i | N_1 \in tet_i, i = 1 \sim n_1\} \tag{15}$$

where tet_i is the ith tetrahedral element in group G_1, N_1 is the first node of the failed joint element, and n_1 is the total number of tetrahedral elements in group G_1. It should be noted that here the tetrahedral elements in group G_1 do not really share node N_1 because the space discretisation scheme inserts joint elements between tetrahedral elements (Figure 2). Therefore, the definition of 'sharing node' in the mixed mesh of tetrahedral elements and joint elements is that the nodes have the same initial coordinates before loading starts.

Last, the contact detection algorithm is used to detect contact couples that are in real contact state within and between these six groups of tetrahedral elements $G_1 \sim G_6$. It should be noted that contact couples that still have active joint elements between them are excluded from this detection process. The final detected contact couples can be described as

$$C_{ij} = \left\{ \left(tet_i, tet_j \right) \middle| tet_i \in G_m, tet_j \in G_n, m = 1 \sim 6, n = 1 \sim 6 \right\} \tag{16}$$

The contact scenarios for detected contact couples due to fracturing can be various, e.g. node-node contact, edge-edge contact, edge-face contact, etc. It is worth pointing out that the contact couples listed in Equation 16 only represent the initial contact scenario after new fracture formation. The contact detection algorithm is capable of adaptively searching tetrahedral elements to form and update contact couples; therefore, it gives the computational model the advantage of normal DEM methods to deal with large displacement problems, e.g. sliding and fragmentation.

Once the contact couples are detected, the contact interaction algorithm is used to calculate the contact forces, e.g. normal compression and friction, between fracture surfaces,

and then the contact forces are distributed to the nodes of tetrahedral elements at both sides of the discrete fracture. The contact interaction algorithm used to handle the mechanical contact is based on the penalty function method (Munjiza and Andrews, 2000; Munjiza, 2004). In this algorithm, penetration between discrete elements will generate a pair of contact forces, which are equal in magnitude and opposite in directions, acting on the two elements of a contact couple. The two discrete elements of a contact couple are named contactor and target, respectively (Figure 4).

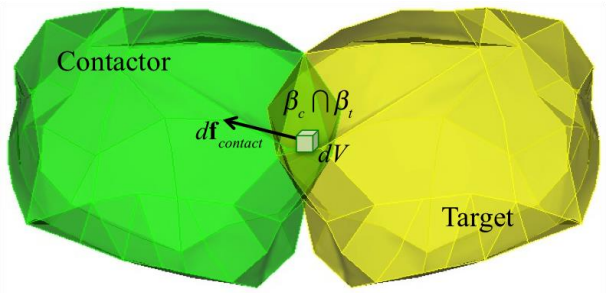

Figure 4: Contact force due to an infinitesimal overlap between a contactor element and a target element.

The contact force $\mathbf{f}_{contact}$ generated due to penetration is then calculated as

$$\mathbf{f}_{contact} = \sum_{i=1}^{m}\sum_{j=1}^{n}\int_{V_{ij}=\beta_{c_i}\cap\beta_{t_j}} \left(grad\varphi_{c_i} - grad\varphi_{t_j}\right) dV_{ij} \tag{17}$$

where dV_{ij} is an infinitesimal overlap between contactor element β_{c_i} and target element β_{t_j}; m and n are the total numbers of tetrahedral elements of the contactor and target, respectively; φ_{c_i} and φ_{t_j} are potential functions for the contactor β_{c_i} and target β_{t_j}, respectively. Sliding friction is also considered as a type of contact by the Coulomb friction law. Sliding in the tangential direction at the contact interface will occur when the tangential contact force is greater than μN, where μ is the friction coefficient, and N is the normal pressure at the contact interface.

It should be noted that the contact forces are only calculated between tetrahedral elements when they are found as a contact couple by the contact detection algorithm. More specifically, before fracture formation the tetrahedral elements are purely connected by joint elements,

which contribute to the nodal forces $\mathbf{f}_{joint}$. After fracture formation, $\mathbf{f}_{joint}$ becomes zero as the formation of fractures is determined upon the failure of joint elements; instead, a contact force $\mathbf{f}_{contact}$ will be calculated between tetrahedral elements at both sides of the failed joint element. The smooth transition from continuum to discontinuum therefore relies on the switch from $\mathbf{f}_{joint}$ to $\mathbf{f}_{contact}$. When a tensile fracture is formed, $\mathbf{f}_{joint}$ has already diminished to zero and the initial $\mathbf{f}_{contact}$ equals zero as well due to zero overlap between tetrahedral elements – as they moved apart in tension, so a smooth transition is guaranteed. However, when a shear fracture under normal compression is formed, the overlap between tetrahedral elements due to compression will generate an initial non-zero contact force $\mathbf{f}_{contact}^{initial}$, which can cause instability problems because a zero $\mathbf{f}_{joint}$ is suddenly replaced by a non-zero $\mathbf{f}_{contact}^{initial}$. In order to achieve a smooth transition, a ramping function is applied to gradually increase the contact force to its initial value,

$$\mathbf{f}_{contact} = \frac{n_c}{n_{total}} \mathbf{f}_{contact}^{initial} \tag{18}$$

where n_c is the current time-step, which is locally defined only for the calculation of contact forces and starts from zero when a shear fracture is formed; n_{total} is the total time-steps for n_c (usually 10). Once the initial value is reached, the contact force will be calculated as normal using Equation 17.

2.4 Discretised equilibrium equations

In the three-dimensional fracturing simulations, the domain is discretised by 4-node tetrahedral elements and 6-node joint elements. The motions of element nodes are governed by internal forces and external forces acting on them. The governing equation for each individual node is given as

$$m_i \dot{\mathbf{v}}_i + \mathbf{f}_{int} = \mathbf{f}_{ext} \tag{19}$$

where m_i is the mass of node i; $\dot{\mathbf{v}}_i$ is the acceleration vector of node i; $\mathbf{f}_{int}$ is the internal force vector of node i; $\mathbf{f}_{ext}$ is the external force vector of node i. The internal force $\mathbf{f}_{int}$ is calculated from stresses in tetrahedral elements and the external force $\mathbf{f}_{ext}$ includes three parts,

$$\mathbf{f}_{ext} = \mathbf{f}_{joint} + \mathbf{f}_{contact} + \mathbf{f}_{load} \tag{20}$$

where $\mathbf{f}_{joint}$ is the external force vector contributed by the stresses in joint elements; $\mathbf{f}_{contact}$ is contributed by the contact interaction in the DEM formulation; $\mathbf{f}_{load}$ is contributed by external loading, such as body force and surface traction. A Forward Euler method (FE) is used for explicit time integration.

3 Numerical examples

In this section, the computational model is applied to three numerical tests. First, the Brazilian test, i.e. diametral compression of a disc specimen, is chosen to examine the capability of the three-dimensional fracture model to simulate tensile fractures with minor shear fractures in indirect tensile stress fields. Second, the polyaxial or true-triaxial compression test, in which a cube specimen is compressed in orthogonal three-dimensional stress conditions, is simulated to investigate shear fracturing behaviour. Third, a realistic three-dimensional multi-layer rock model is simulated under an *in situ* stress condition as an example of applying the computational model for engineering problems. It should be noted that the materials of all the models presented in this section are assumed to be isotropic and homogeneous.

3.1 Brazilian test

3.1.1 Test setup

The setup for the Brazilian tests is shown in Figure 5. A vertically placed disc specimen perpendicular to the *z*-direction is compressed diametrally between two platens placed horizontally. The diameter of the disc specimen is 40 mm and the thickness in the *z*-direction is 15 mm (Figure 5a). Loading velocities V_y in the vertical *y*-direction are applied to the two platens to generate an indirect tensile stress field in the disc specimen. The upper platen moves downwards and the lower platen moves upwards at the same velocity. The value of loading velocity V_y is defined by a ramping curve, which means the velocity first increases linearly from zero to a constant value V_y, and then keeps constant for the rest of the simulation time. This ramping function is mainly designed to reduce the impact effect when the loading starts. It should be noted that there are no pre-existing flaws in the disc specimen (Figure 5b).

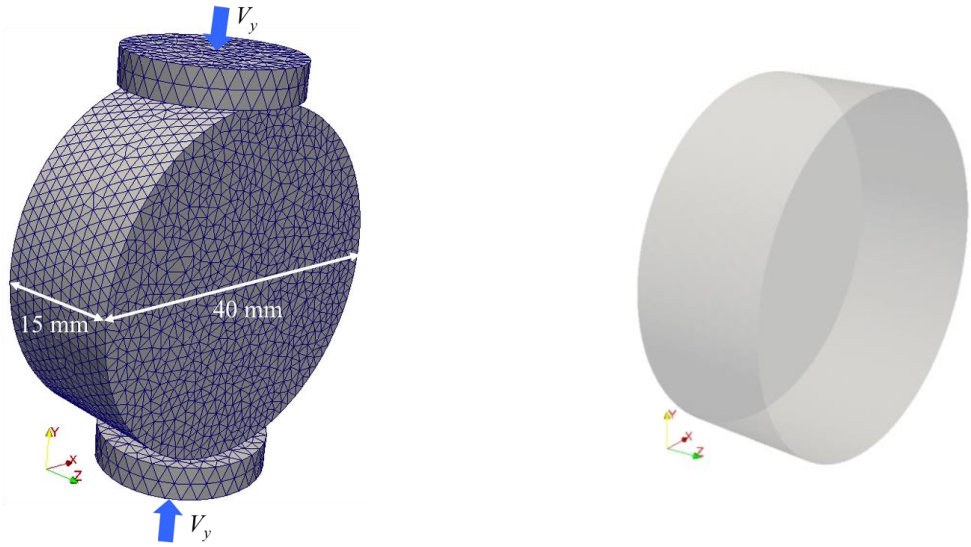

a. Dimensions, mesh and loading condition of the model.

b. Inside of the disc specimen. Note that there are no pre-existing flaws.

Figure 5: Test setup of Brazilian tests.

The material used for the disc specimen (Table 1) is assumed to represent typical rock (Lama and Vutukuri, 1978; Atkinson, 1987; Zoback, 2010) or fine concrete mortar properties (Popovics, 1998) and the platens are assumed to be made of steel. It should be noted that the fracture model is only applied to the disc specimen, and the steel platens are assumed to be rigid, which means there is no deformation in the platens, so material properties are not needed for them. The platens are only meshed for convenience reasons in the mesh creation; the actual mesh is not involved in the stress calculations (Mahabadi et al., 2010). The friction coefficient is set to be 0.6 between fracture surfaces, and 0.1 between the disc specimen and platens. The domain is meshed using unstructured 4-node tetrahedral elements and the mean mesh size is ~ 1.2 mm, which satisfies mesh convergence criteria (Guo et al., 2016). A total number of 51690 elements are generated for the disc specimen and 2854 elements for the platens. The time-step used in the simulations is $\Delta t = 2 \times 10^{-9}$ s.

Table 1: Material properties in the Brazilian tests.

Material properties	Values
Density ρ (kg·m^{-3})	2340
Young's modulus E (GPa)	26
Poisson's ratio υ	0.2
Tensile strength f_t (MPa)	3
Cohesion c (MPa)	15
Internal friction angle ϕ (°)	30
Fracture energy G_f (J·m^{-2})	50

3.1.2 Numerical results

Four loading velocities are tested for the same disc specimen in the Brazilian tests. The aim is to investigate the dynamic effect of different loading rates on the indirect tensile strength. The load F and vertical strain ε_{yy} obtained from numerical simulations are plotted in Figure 6 for loading velocities V_y = 0.1, 0.05, 0.02 and 0.01 m/s. Since the upper and lower platens both move at the same velocity but in opposite directions, the load F is calculated as

$$F = \frac{1}{2}\left(F_{upper} + F_{lower}\right) \tag{21}$$

where F_{upper} is the contact force between the upper platen and the disc specimen; and F_{lower} is the contact force between the lower platen and the disc specimen. The vertical strain ε_{yy} of the disc specimen is defined by

$$\varepsilon_{yy} = \frac{\Delta a}{d} \tag{22}$$

where d is the diameter of the disc specimen.

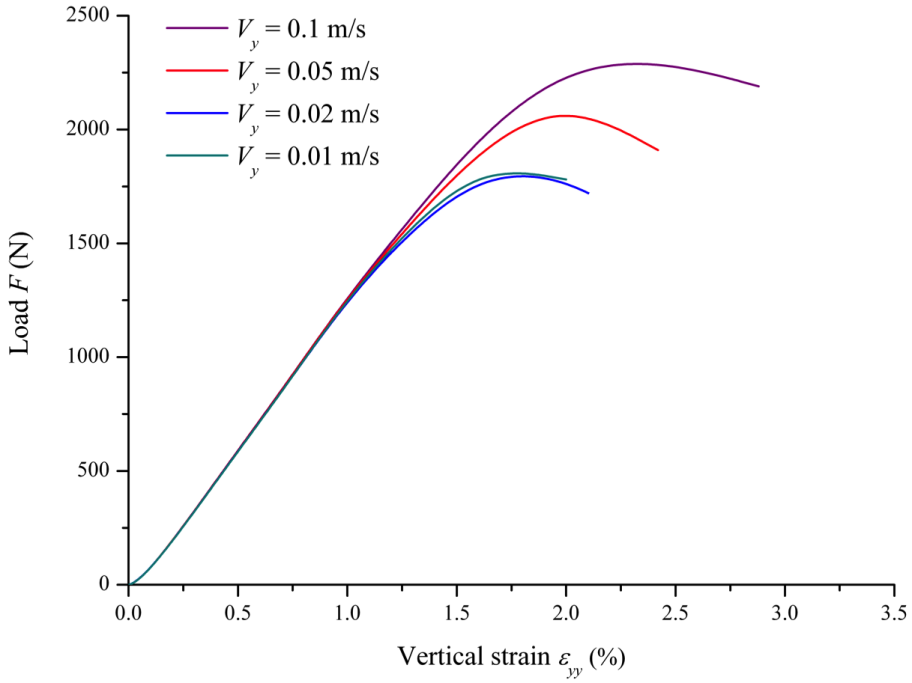

Figure 6: Plots of load F versus vertical strain ε_{yy} of the disc specimen in Brazilian tests.

It can be seen from Figure 6 that the peak load of the disc specimen drops as the loading velocity decreases. However, it is found that the peak loads obtained from loading velocities V_y = 0.02 and 0.01 m/s are almost the same, which indicates these velocities can represent quasi-static loading conditions. It is known from Figure 6 that the peak load corresponding to loading velocity V_y = 0.01 m/s is F = 1844.76 N, so the indirect tensile strength f_{bt} can be calculated by Equation 23.

$$f_{bt} = \frac{2F}{\pi dt} \tag{23}$$

where d is the diameter of the disc specimen, d = 0.04 m; and t is the thickness, t = 0.015 m (Figure 5a), so the calculated indirect tensile strength is f_{bt} = 1.96 MPa. It is worth noting that the indirect tensile strength obtained from the numerical simulation is smaller than the input value of tensile strength f_t = 3 MPa (Table 1). This discrepancy might be explained by the difference between the direct tensile strength and the indirect tensile strength. The input tensile strength as a material property is used in the fracture model as a concept of direct tensile strength, which is different from the indirect tensile strength in terms of the definitions and the experiment methods used to obtain them. More specifically, the direct tensile strength

is obtained from direct tension tests, i.e. pulling a bar specimen, which are normally difficult for quasi-brittle materials, as they break without significant deformation and the two ends clamped by experimental equipment can easily crush. The indirect tensile strength is obtained typically from Brazilian tests, which are better controlled for quasi-brittle materials. Fairhurst (Fairhurst, 1964) concluded that a Brazilian test would underestimate tensile strength for a rock with a low ratio of compressive to tensile strength when the contact areas between the loading platens and the specimen are small. In the numerical tests presented here, the two loading platens both have planar surfaces in contact with the disc specimen, which results in narrow strips of contact areas and localised contact forces. Because the material shear strength is not sufficiently high to resist the localised and concentrated contact forces at the two ends of the disc specimen, the disc fails in both tensile mode (centre of the disc specimen) and shear mode (two ends in contact with the platens). Therefore, the structure resistance to the loading is underestimated.

The numerical results of loading velocity V_y = 0.01 m/s are presented in Figure 7. It can be seen that the simulation obtains correct stress fields and fracture patterns that match theoretical predictions (Fairhurst, 1964). Before fracture initiation, tensile stresses are distributed along the vertical diameter of the disc specimen and also there are small areas of compressive stresses distributed near the loading platens (Figure 7a). Due to the high contact forces, shear fractures first initiate at the two ends of the disc specimen that are in contact with the loading platens (Figure 7b). Then the central fracture propagates upwards until it penetrates through the whole disc specimen (Figure 7c – f). It is worth pointing out that in an ideal Brazilian test, the fracture should first initiate at the centre and then propagate outwards. In the future, several improvements can be introduced to achieve more realistic sequence of fracture development, such as material heterogeneity when experimental data is available (Mahabadi et al., 2012, 2014) and plasticity deformation for more accurate energy dissipation.

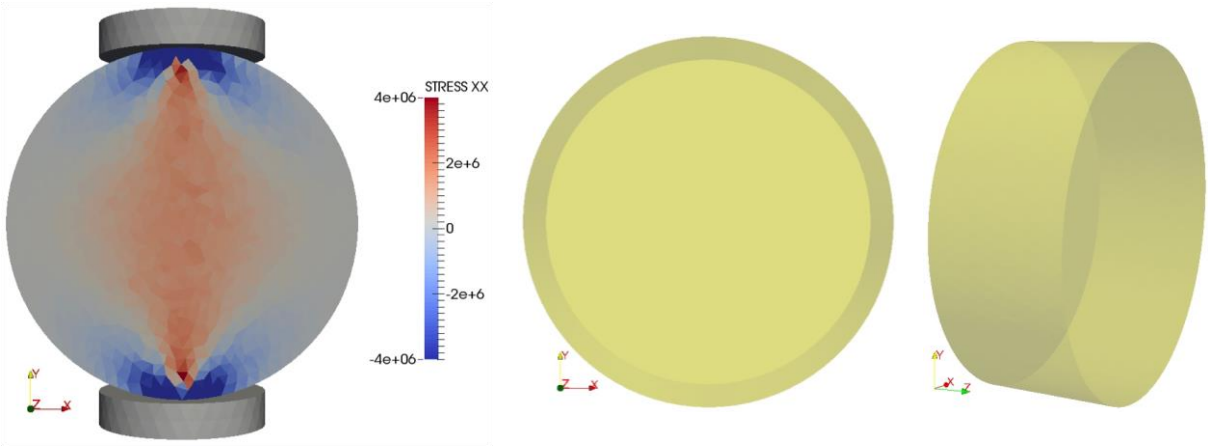

a. Vertical strain ε_{yy} = 1.03%.

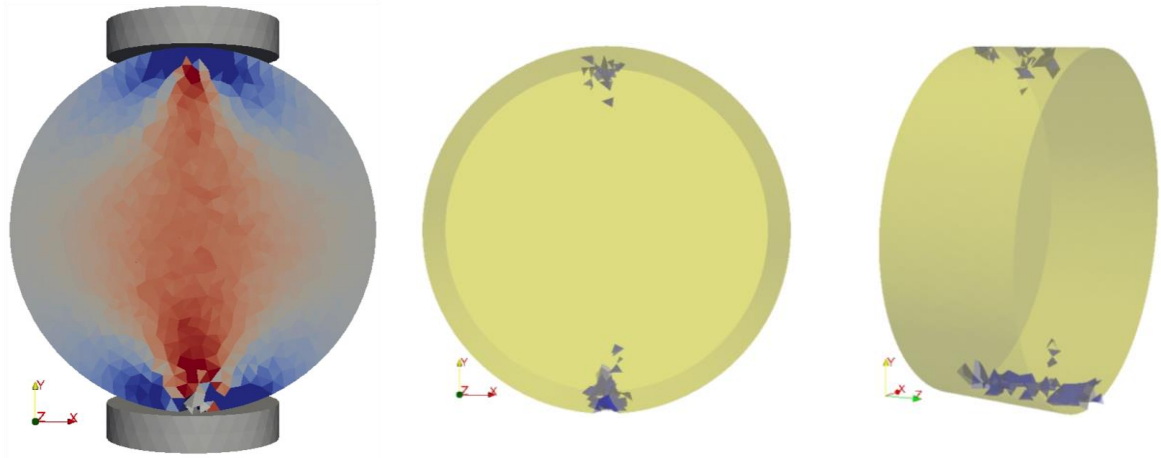

b. Vertical strain ε_{yy} = 1.59%.

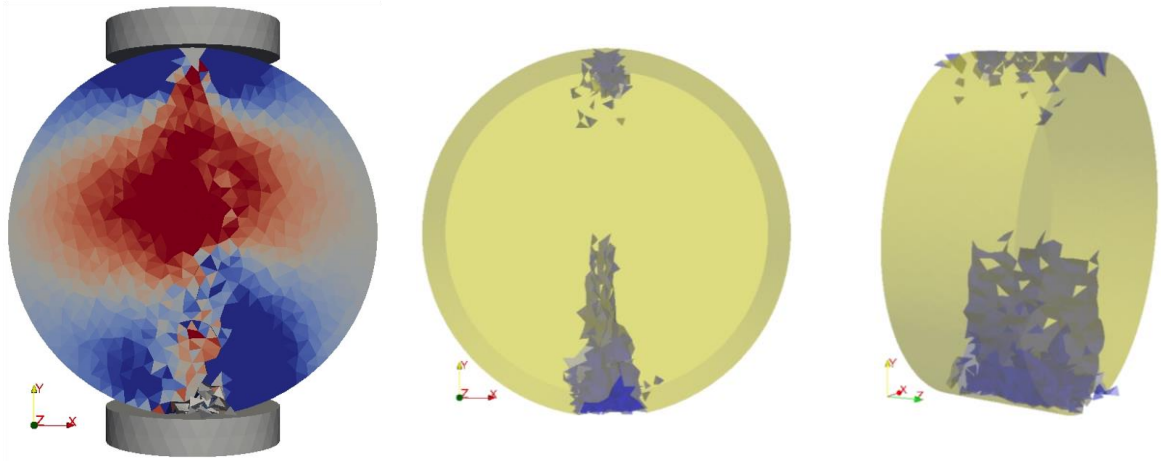

c. Vertical strain ε_{yy} = 3.11%.

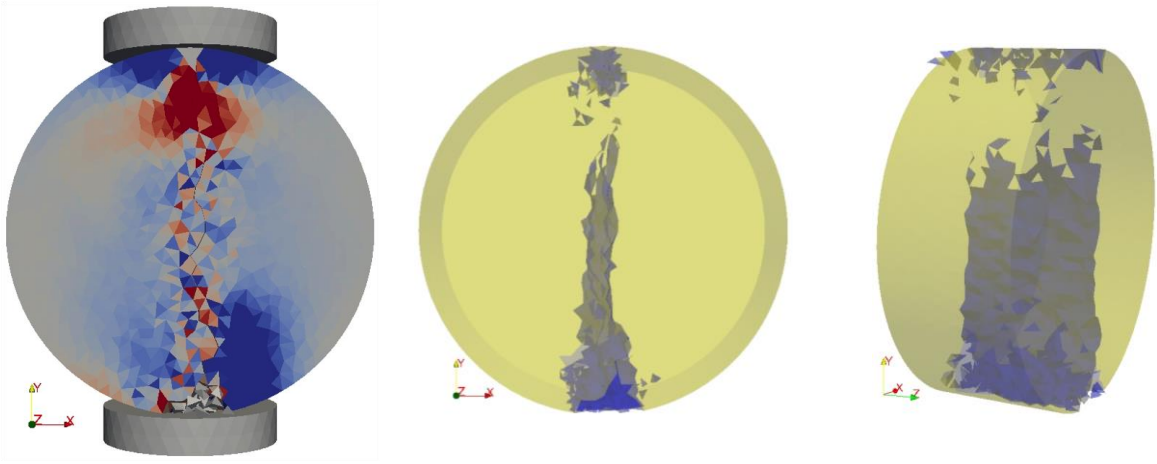

d. Vertical strain ε_{yy} = 3.15%.

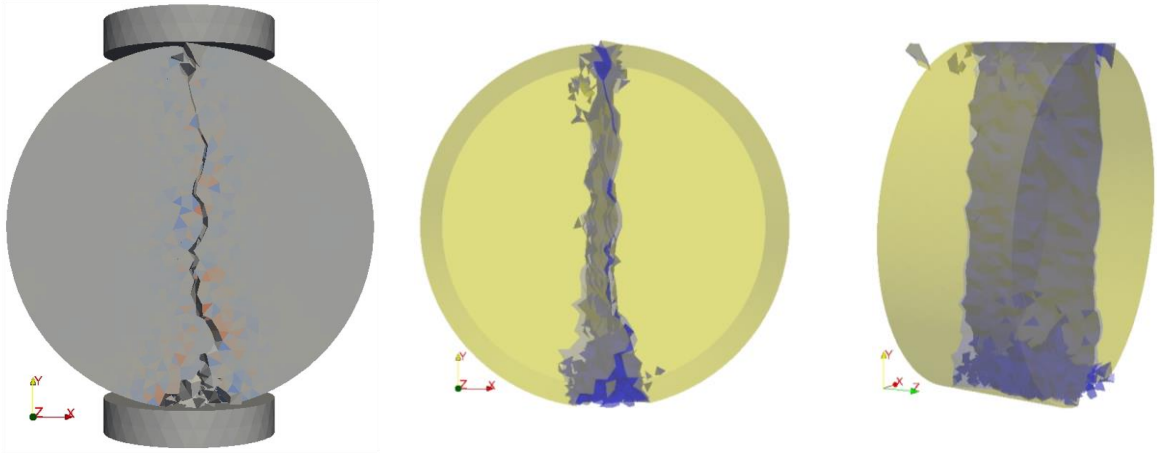

e. Vertical strain ε_{yy} = 4.01%.

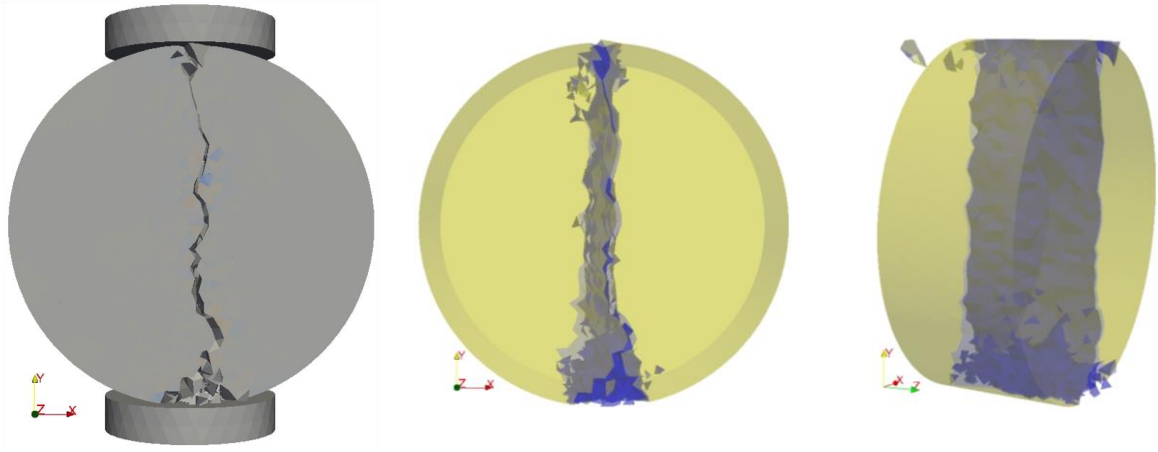

f. Vertical strain ε_{yy} = 4.15%.

Figure 7: Numerical results of Brazilian tests at loading velocity V_y = 0.01 m/s. The left-hand column shows the horizontal stress components (tensile direction). The fracture patterns are viewed from the positive *z*-direction (the middle column) and in three-dimensional views (the right-hand column).

Final fracture patterns of loading velocities V_y = 0.01 and 0.05 m/s are compared in Figure 8. They both have major tensile splitting fractures in the middle of the disc specimen and minor crushing zones (shear fractures) near the two ends that are in contact with the loading platens, which are similar to fractures obtained from laboratory experiments (Guo et al., 1993).

a. V_y = 0.01 m/s. b. V_y = 0.05 m/s.

Figure 8: Comparison of final fracture patterns in Brazilian tests obtained from two loading velocities V_y = 0.01 and 0.05 m/s.

3.2 Polyaxial compression test

3.2.1 Test setup

The test setup for the polyaxial compression tests is shown in Figure 9. A cube specimen is used as a representation of a homogeneous and isotropic geological unit. The edge length of the cube specimen is 500 mm (Figure 9a) and there are no pre-existing flaws (Figure 9b). Three orthogonal pressure boundary conditions, which represent three principal stresses, are applied to the surfaces of the cube specimen using a ramping function – first increase linearly from zero to a constant pressure, and then remain constant. It is worth noting that this is different from conventional laboratory testing, where the all-round confining pressure is normally applied first so as to allow consolidation, if appropriate, and then the axial pressure is gradually increased until failure happens (Knappett and Craig, 2012). In the numerical tests, the specimen is not assumed to be a porous medium; thus, all of the three orthogonal pressures reach the final constant values simultaneously, but the values are different. As a result, the slopes of linear increases (incremental stresses) are not the same. Different slopes

have been tested to make sure the final stresses can represent a quasi-static failure state. It should be noted that here the engineering mechanics sign convention is used, so tensile stress is positive and compressive stress is negative, and the three principal stress components are in the order of $\sigma_1 \geq \sigma_2 \geq \sigma_3$.

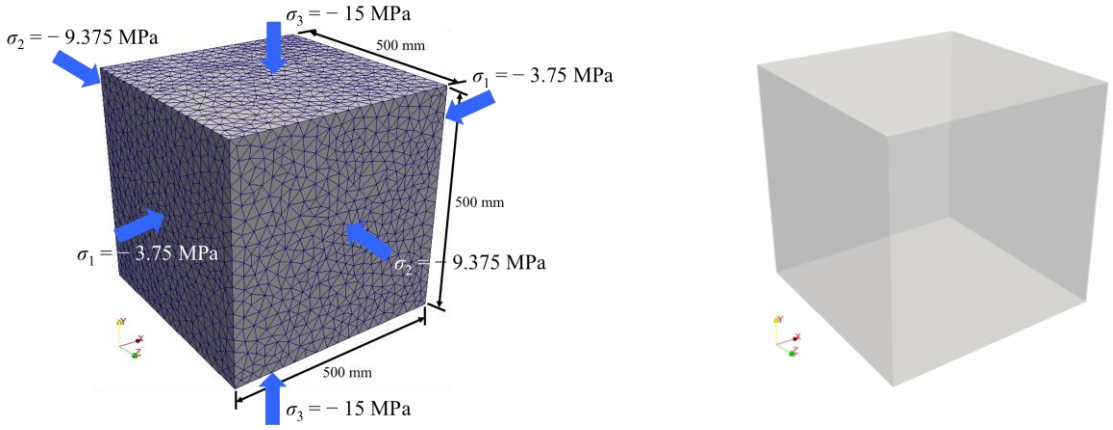

a. Dimensions, mesh and loading condition of the model.

b. Inside of the cube specimen. Note that there are no pre-existing flaws.

Figure 9: Test setup of polyaxial compression tests.

The material of the cube specimen in the polyaxial compression tests (Table 2) is assumed to represent typical limestone (Engelder and Peacock, 2001; Zoback, 2010). A friction coefficient equal to 0.6 is assigned on fracture surfaces. The whole cube domain is meshed by unstructured 4-node tetrahedral elements. The mean mesh size is ~ 27 mm (smallest mesh element size ~ 17 mm) and a total number of 55435 elements are generated. The time-step in the numerical simulations is $\Delta t = 5 \times 10^{-8}$ s.

Table 2: Material properties in the polyaxial compression test.

Material properties	Test 1	Test 2	Test 3
Density ρ (kg·m^{-3})	2700	2700	2700
Young's modulus E (GPa)	30	30	30
Poisson's ratio υ	0.27	0.27	0.27
Tensile strength f_t (MPa)	1.0	1.0	1.0
Cohesion c (MPa)	0.5	2.0	3.8
Internal friction angle ϕ (°)	33.4	23.8	12.4
Fracture energy G_f (J·m^{-2})	60	60	60

3.2.2 Numerical results

Three sets of material properties are tested in the polyaxial compression tests. The aim is to compare three different materials in identical stress states but have inherently different strength related properties. Therefore, the only difference between the three materials is the cohesion c and the internal friction angle ϕ, which are listed as follows:

Test 1: c = 0.5 MPa, ϕ = 33.4° (tanϕ = 0.66);

Test 2: c = 2.0 MPa, ϕ = 23.8° (tanϕ = 0.44);

Test 3: c = 3.8 MPa, ϕ = 12.4° (tanϕ = 0.22).

It should be noted that the internal friction angle in the third test (ϕ = 12.4°, tanϕ = 0.22) is not a very realistic value for rock material (Zoback, 2010). The main reason for choosing this value is to investigate the shear fracturing behaviour at three consecutively halving tangents of the internal friction angles (0.66, 0.44 and 0.22). For the purpose of testing different materials in the same stress state, the pressure boundary conditions are the same for all of the three tests.

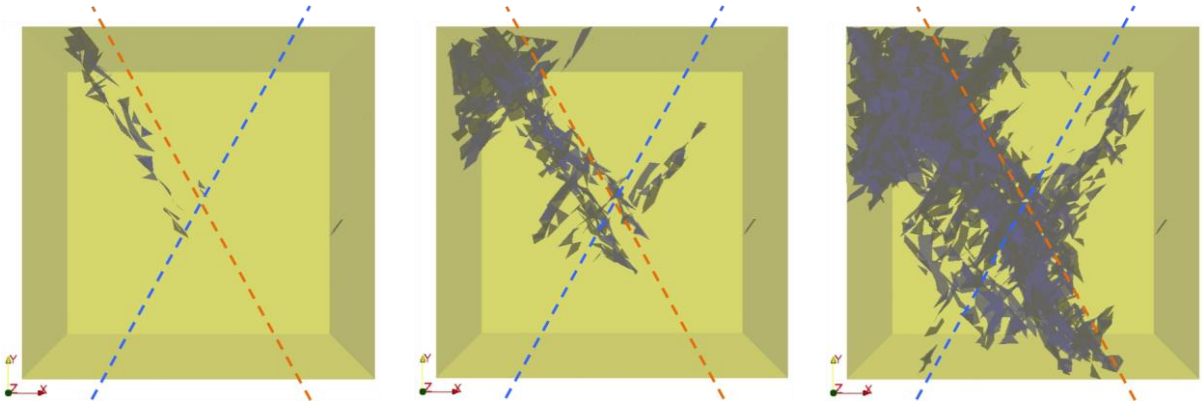

a. Initial shearing. b. Conjugate shearing. c. Final pattern.

Figure 10: Shear fracture formation in the polyaxial compression test with material properties of c = 0.5 MPa and ϕ = 33.4° (tanϕ = 0.66). Note that the orange dashed lines show the main shear direction and the blue dashed lines show the symmetric complementary conjugate direction.

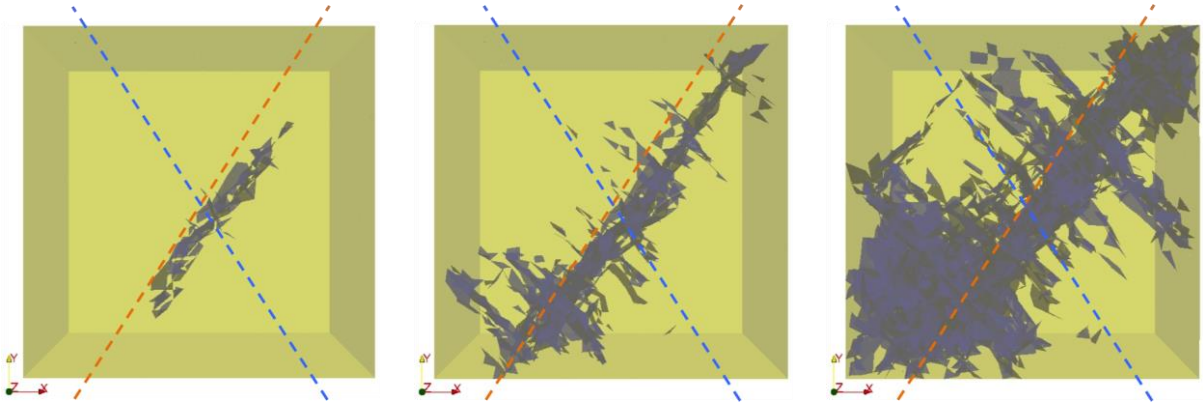

a. Initial shearing. b. Conjugate shearing. c. Final pattern.

Figure 11: Shear fracture formation in the polyaxial compression test with material properties of c = 2.0 MPa and ϕ = 23.8° (tanϕ = 0.44).

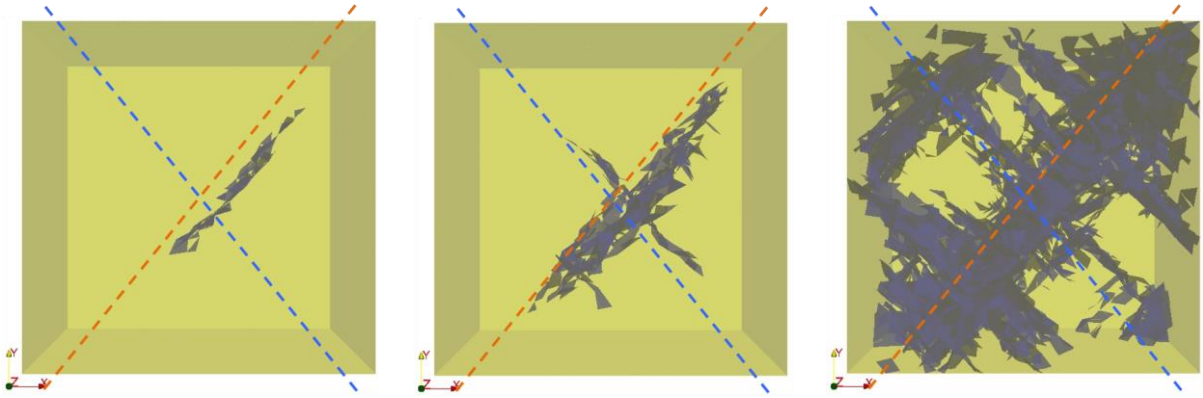

a. Initial shearing. b. Conjugate shearing. c. Final pattern.

Figure 12: Shear fracture formation in the polyaxial compression test with material properties of c = 3.8 MPa and ϕ = 12.4° (tanϕ = 0.22).

The shear fracture development obtained from numerical simulations is shown in Figure 10, Figure 11 and Figure 12. It should be noted that the orange and blue dashed lines in these figures represent the symmetric conjugate shearing directions, which have an angle of ± 45° ± ϕ/2 with the direction of the minimum compressive stress (horizontal direction) according to the Mohr-Coulomb theory. For example, for the first test of c = 0.5 MPa and ϕ = 33.4° (Figure 10), one of the theoretical shear directions (orange dashed line) is

$$-45° - \frac{\phi}{2} = -61.7° \tag{24}$$

It can be seen from Figure 10, Figure 11 and Figure 12 that the shear directions obtained from numerical simulations are in good agreement with the theoretical directions. It should be

noted that non-associated flow rules are normally used for soil, rock and concrete, etc., in which the inclination of the shear bands should consider the dilatancy angle ψ as well (Arthur et al., 1977; Vardoulakis, 1980), therefore,

$$\alpha = 45° + (\phi + \psi)/4 \tag{25}$$

The dilatancy angle ψ is at least 20° less than the friction angle ϕ (Vermeer and de Borst, 1984). However, previous research found that the shear bands in fine sands tended to develop at the Coulomb direction (Vermeer, 1990). Lade and Wang (2001) also found that in dense sands the shear band inclinations compared more favorably with the Coulomb direction. The material for the numerical tests here is assumed to be rock or concrete without microstructures, which can be assumed to be equivalent to a specimen of densely packed fine granular material; therefore, the shear band inclination angle is estimated purely based on the Mohr-Coulomb criterion.

At the initial stages (Figure 10a, Figure 11a and Figure 12a), shear fractures initiate and propagate to make a macroscopic shear fracture (orange dashed lines) at an angle as predicted by the Mohr-Coulomb theory and in accordance with the element scale criteria implemented for failure on joint elements. Then several sets of small shear fractures develop in the complementary conjugate directions (blue dashed lines) to the first set of shear fractures (Figure 10b, Figure 11b and Figure 12b), and these first three or four significant conjugate shears grow to compensate for the strain caused by the sliding on the first macroscopic shear. The final shear fracture patterns in Figure 10c, Figure 11c and Figure 12c show a main set of continuous shear fractures through the entire cube specimen and several sets of small shear fractures orientated in the conjugate directions to the main originally formed set.

In our simulations, the specimen can be assumed to be equivalent to a very densely packed specimen of granular material, in which the failure is normally observed as localised shear bands (Wang and Lade, 2001; Guo and Zhao, 2016a). It is worth pointing out that if the specimen is loosely packed, the failure mode is more like a diffused pattern (di Prisco et al., 1997; Chu and Leong, 2002; Lade, 2002; Khoa et al., 2006; Daouadji et al., 2010). Generally speaking, in granular materials failure may occur in a localised pattern (shear band) or a diffused pattern (uniform peak) (Wang and Lade, 2001; Huang et al., 2007). The final failure

pattern can be explained as the result of self-organisation of multiple fractures – a balance between competing processes, such as a reaction process to localise fractures and a diffusion process to homogenise fractures (Ord and Hobbs, 2010).

The material properties and loading pressures in the polyaxial compression tests are specially chosen to make sure the cube specimen breaks in a manner predicted by the Mohr-Coulomb theory. The Mohr circle representing the applied principal stresses and three Mohr-Coulomb failure envelopes corresponding to three sets of material properties are plotted in Figure 13. It can be seen that the Mohr circle just touches all the three failure envelopes, which means the applied principal stresses are just sufficient to cause the cube specimen to fail according to the Mohr-Coulomb theory. The numerical results match these theoretical predictions very well.

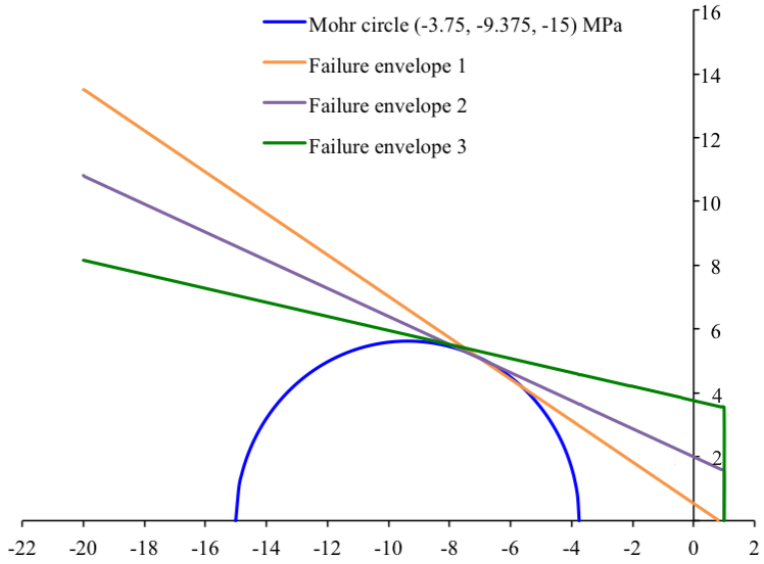

Figure 13: Mohr circle and Mohr-Coulomb failure envelopes in the polyaxial compression tests. Note that the Mohr circle reprents the principal stresses ($\sigma_1 = -3.75$ MPa, $\sigma_2 = -9.375$ MPa, $\sigma_3 = -15$ MPa) applied to the cube specimen. The three Mohr-Coulomb failure envelopes correspond to three sets of material properties: $c = 0.5$ MPa and $\phi = 33.4°$, $c = 2.0$ MPa and $\phi = 23.8°$, $c = 3.8$ MPa and $\phi = 12.4°$, respectively.

It is worth mentioning that the shear-failure-dominated fracture patterns obtained using the computational model in the polyaxial compression tests are not as clean as the tensile-failure-dominated fracture patterns obtained in the Brazilian tests. In the tensile-failure-dominated fracture patterns, the major tensile fractures usually propagate without many

branches, and therefore have continuous and clean fracture surfaces. In the shear-failure-dominated fracture patterns, however, multiple small shear fractures form at the same time, and then these fractures propagate and coalesce to form shear bands, which have multiple shear fractures distributed in narrow strips. This difference between tensile and shear failure modes is more significant when shear failure happens in compressive stress fields (Lockner et al., 1991), like the polyaxial compression presented in this section.

3.3 Three-dimensional multi-layer model

In this section, an example is presented as an application of the computational model to reservoir modelling in petroleum engineering. Naturally fractured reservoirs are an important source of hydrocarbons. The difficulty in characterising such reservoirs is mainly attributed to the lack of sufficient sub-surface data to create realistic fracture network models (Nelson, 2001). Understanding mechanisms and processes of fracture pattern formation can help predict fracture characteristics in different stress regimes. A considerable amount of research has been done on the tectonic setting and stress regimes that exist in the Earth's crust, and the brittle and ductile structures that are produced in sedimentary rock as a consequence. A good discussion of the mechanical principles and concepts used to analyse geological structures can be found in the book by Price and Cosgrove (1990).

One study area of great importance is the research of fracture development in relation to multi-layered rock to understand the role of fractures in vertical fluid migration across and within sedimentary rock layers. Sedimentary sequences in reservoir basins at different stages in their geological evolution to the present day may have been exposed to phases of deformation involving both layer extension and layer compression. Previous research on layered rock (Wu and Pollard, 1995) concluded that opening-mode tensile fractures are a common occurrence, and these are often confined and terminated by layer boundaries. However, sometimes through-going fractures are observed which penetrate many layer boundaries. The mechanisms allowing this significant pathway for fluids are not well understood and are the subject of great interest to structural geologists and reservoir engineers concerned with the integrity of cap rock.

The objective of the third numerical example is to apply the computational model to mechanically simulate the growth of realistic fracture patterns in three-dimensional layered rock. Some previous work by the authors looked at a similar problem in two dimensions (Guo et al., 2017). In this section, the multi-layer rock model and the *in situ* stress condition are simulated in a true three-dimensional scenario, and three-dimensional fracture pattern development, which is associated with stress heterogeneity and stress concentration, is investigated.

3.3.1 Model setup

The model simulated here is generated by extruding a two-dimensional fracture network, which is a section of 1.5 m × 1.5 m from a realistic two-dimensional fracture pattern map (see the green box in Figure 14). The extracted fracture pattern originally is a fracture map of one near horizontal limestone horizon exposed in a wave cut platform. In order to simulate interactions between fracture walls, a duplicate line is created along each fracture and the number of duplicate nodes at intersections depends on the local fracture patterns. To build a three-dimensional model, first it has been put vertical so gravity acts normal to one of the discontinuity sets – the most persistent set – that to aid interpretation may be viewed as if it was the bedding plane or sedimentary layering direction. This two-dimensional fracture pattern is then extruded in the out-of-plane direction (perpendicular to the original map) by 0.5 m (Figure 15a). The fracture distribution inside the model can be seen by using a semi-transparent colour scheme in Figure 15b. There are two major sets of fractures in this model, along the layering direction are persistent fractures, which may be viewed as if they are the layer interfaces separating beds of identical intact rock; the other set are non-persistent fractures, some of which terminate at layer interfaces and some are connected through several layers.

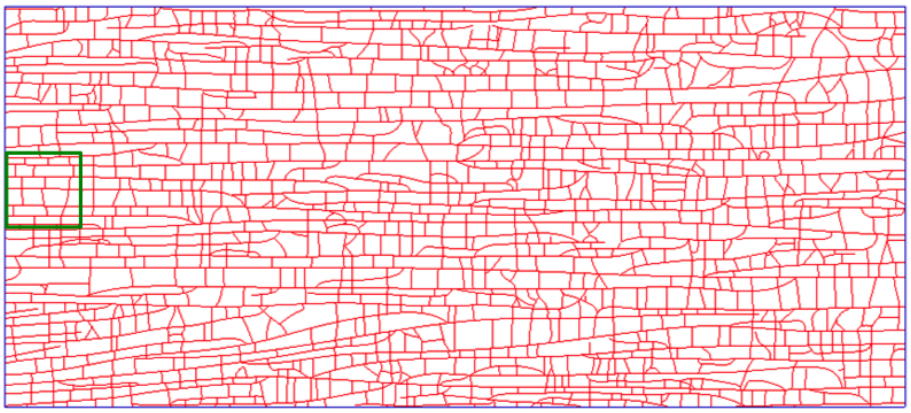

Figure 14: Fracture pattern mapped from the Bristol Channel Basin (after Belayneh and Cosgrove, 2004). The green box shows the extracted section of 1.5 m × 1.5 m.

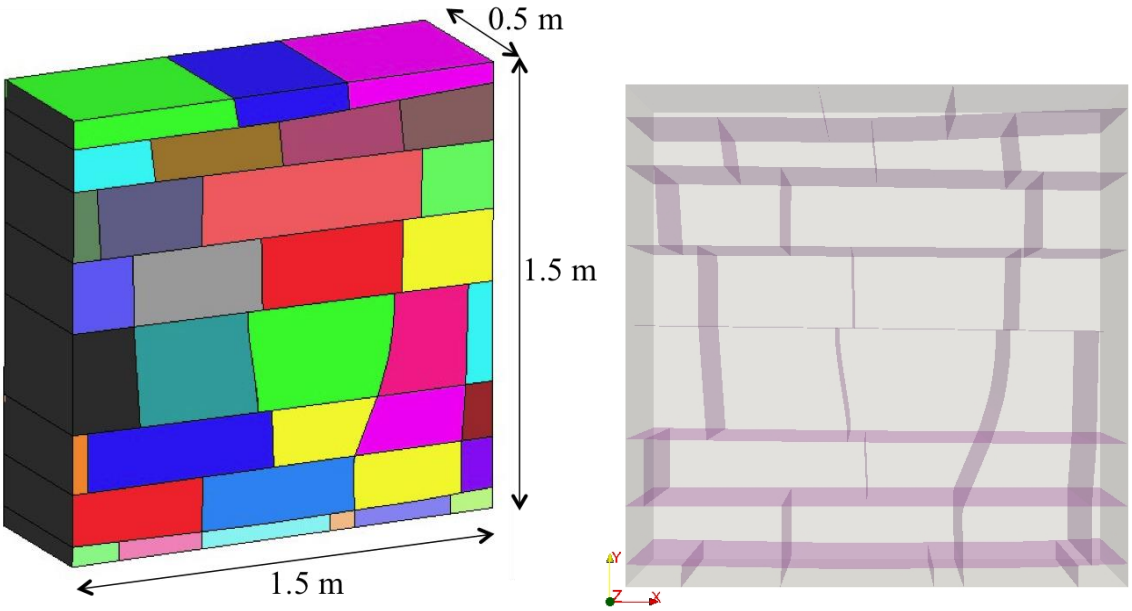

a. Dimensions of the three-dimensional multi-layer model. Different colours represent different units.

b. Fracture distribution inside the three-dimensional multi-layer model. The semi-transparent grey colour represents the outer boundary of this model, and the purple colour represents original fracture surfaces.

Figure 15: Dimensions and fracture distribution of the three-dimensional multi-layer model.

Pressure boundary conditions are applied to all six boundary surfaces (Figure 16). The two surfaces perpendicular to the *x*-direction have traction $P_x = \sigma'_1 = 2.5$ MPa; the two surfaces perpendicular to the *z*-direction have pressure $P_z = \sigma'_2 = -7.5$ MPa; the two surfaces perpendicular to the *y*-direction have pressure $P_y = \sigma'_3 = -15$ MPa. This set of effective

principal stress data has taken fluid pressure into account and is designed to represent an *in situ* effective stress condition. The acceleration of gravity g is set to be 9.8 m/s^2, which acts in the negative y-direction. It is worth mentioning that the direction of gravity has no significant effect on the deformation that is modelled as the scale and rate of boundary condition does not permit body force at the top and the bottom of the model to be significantly different.

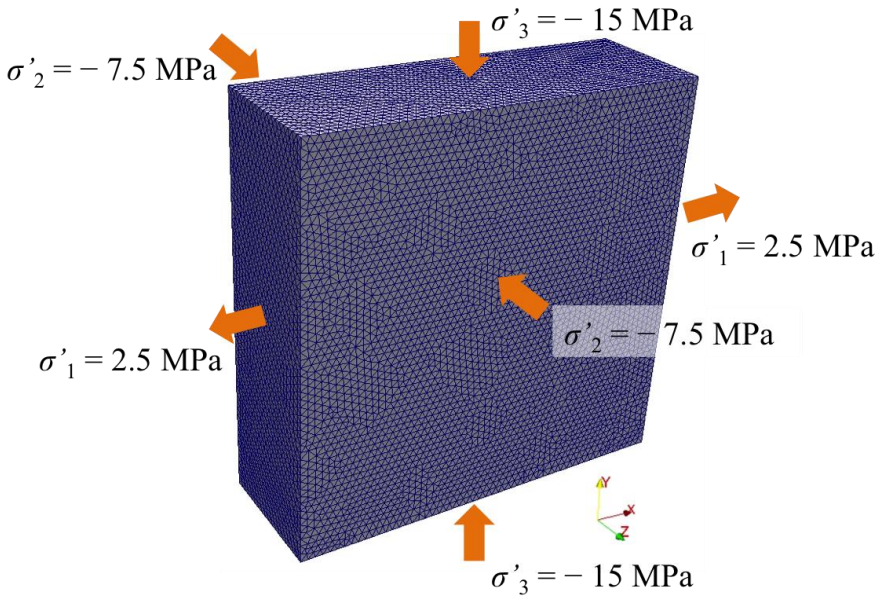

Figure 16: Mesh and the *in situ* stress condition for the three-dimensional multi-layer model.

The rock properties assigned to this model are assumed to be representative of typical limestone (Zoback, 2010; Engelder and Peacock, 2001). The material properties are listed in Table 3. The friction coefficient μ is set to be 0.6 at layer interfaces and fracture surfaces.

Table 3: Material properties used in the three-dimensional multi-layer model.

Rock properties	Values
Density ρ (kg·m^{-3})	2700
Young's modulus E (GPa)	60
Poisson's ratio υ	0.35
Tensile strength f_t (MPa)	5.0
Cohesion c (MPa)	12
Internal friction angle ϕ (°)	30
Fracture energy G_f (J·m^{-2})	60

The entire domain is meshed by unstructured 4-node tetrahedral elements (Figure 16). The mean mesh size is approximately 2.4 cm. A total number of 486425 tetrahedral elements are generated. Here a time-step $\Delta t = 5 \times 10^{-8}$ s is used in the simulation.

3.3.2 Numerical results

It can be seen from Figure 17 that all new fractures propagate from existing fracture tips. As stresses build up and amplify at existing fracture tips, the heterogeneity of the stress field increases. When the amplified stresses increase to the material strength, fractures start to propagate from these stress concentrations, and the stress concentration zones spread with the propagation of discrete fractures. This fracturing process causes the stress heterogeneity in the model to change all the time, though the exact relation between degree of fracturing and stress heterogeneity is not clear yet. It can also be seen that this heterogeneous stress field mostly generates tensile fractures with a few minor shear fractures as well. For example, in the middle-right area, the upper end of an existing fracture first propagates into the neighbouring layer as a tensile fracture, and then bifurcates into two branches as shear fractures.

The original fracture distribution has a significant effect on the formation of new factures since fractures in intact segments are always initiated by stress concentrations around the junctions of layer interfaces and existing fractures. Although this simulation is designed to represent a quasi-static state and the dynamic effects have significantly been reduced by applying the pressure boundary conditions at a very low loading rate, typical transient dynamic phenomena can still be seen from the results. Especially at the early stage of the simulation (Figure 17a-c), the stress contours clearly show the propagation of stress waves from boundaries to the inside and the interaction of stress waves from different directions. The final fracture pattern (Figure 17f), however, can be seen as a stable state because no more new fractures are developed afterwards, and the large stress amplitudes are gradually being reduced by viscous damping (parameter η in Equation 1).

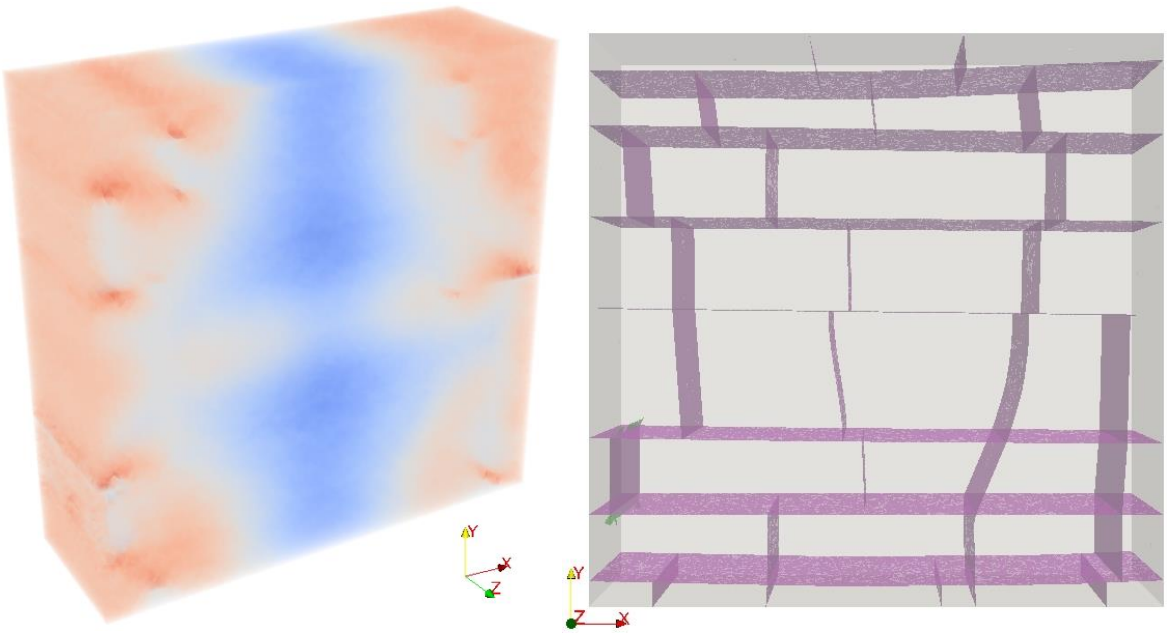

a. 1800 time-steps.

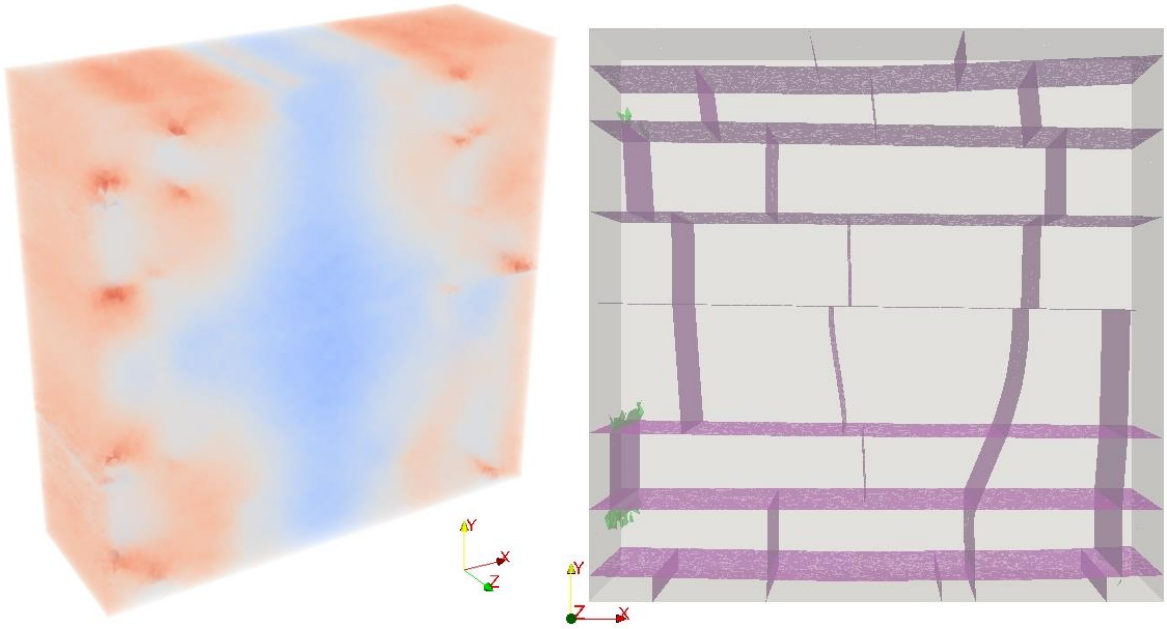

b. 2100 time-steps.

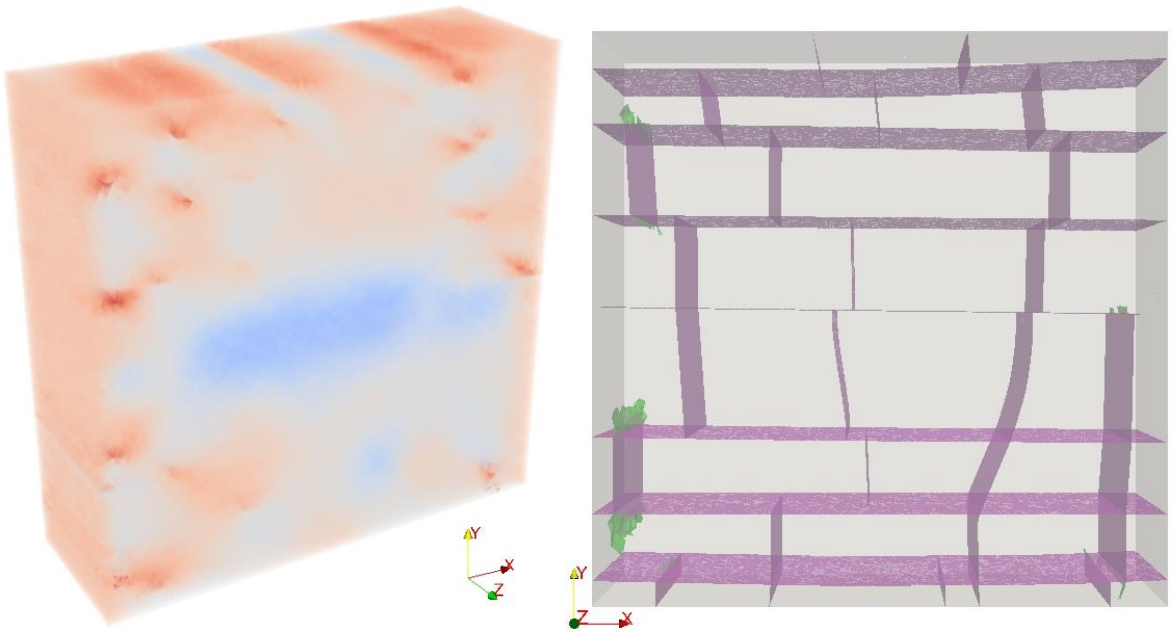

c. 2400 time-step.

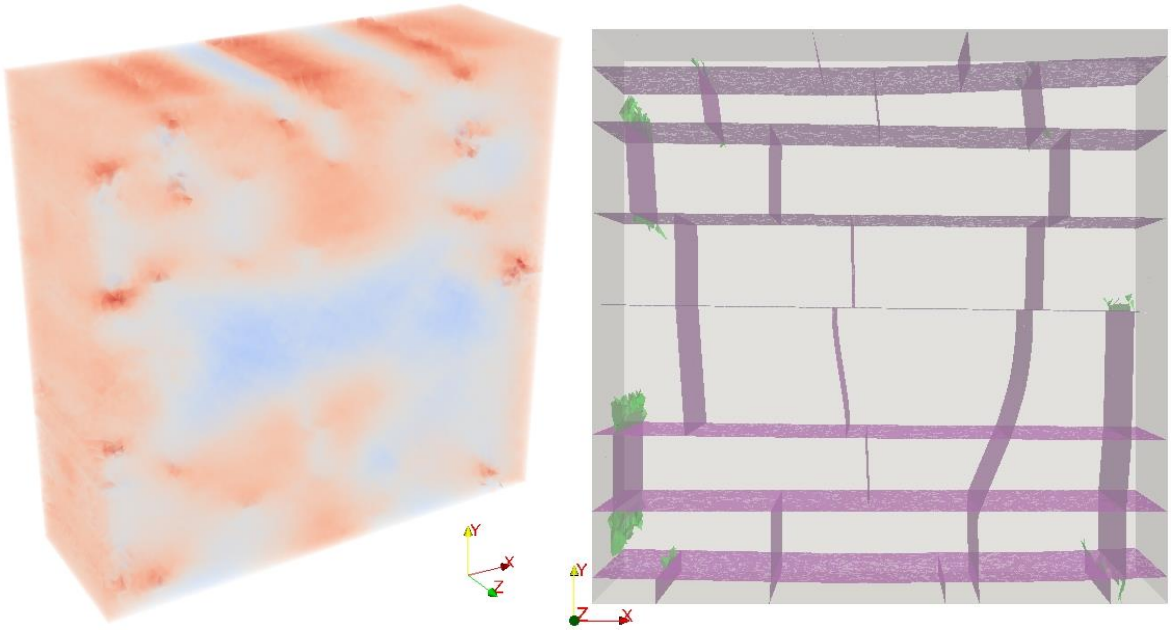

d. 2600 time-steps.

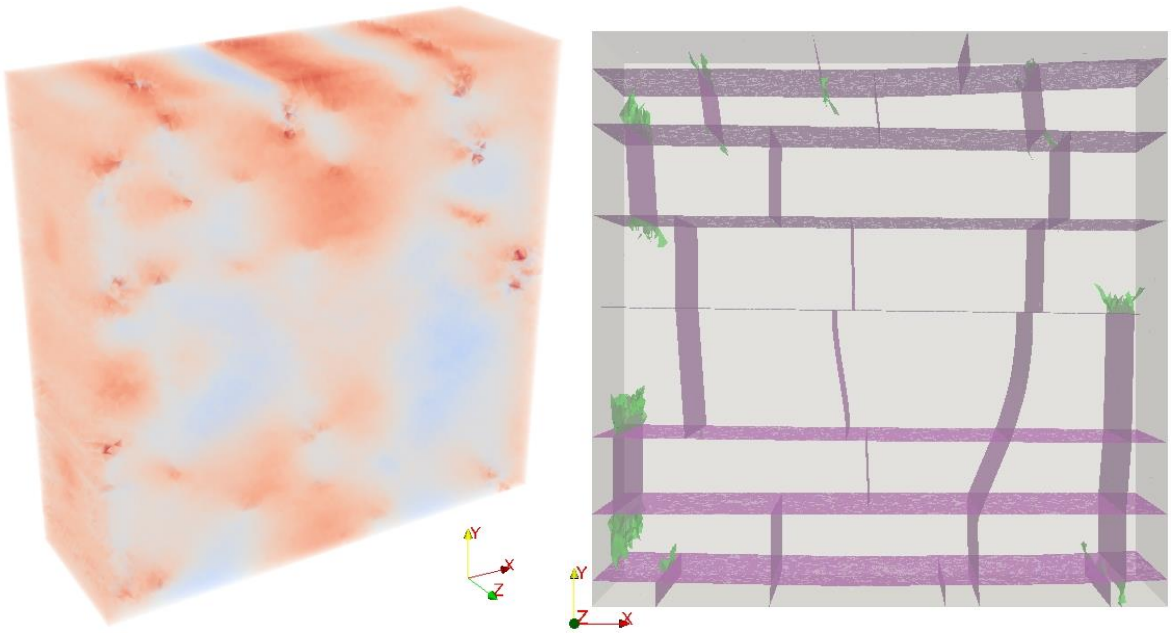

e. 2800 time-steps.

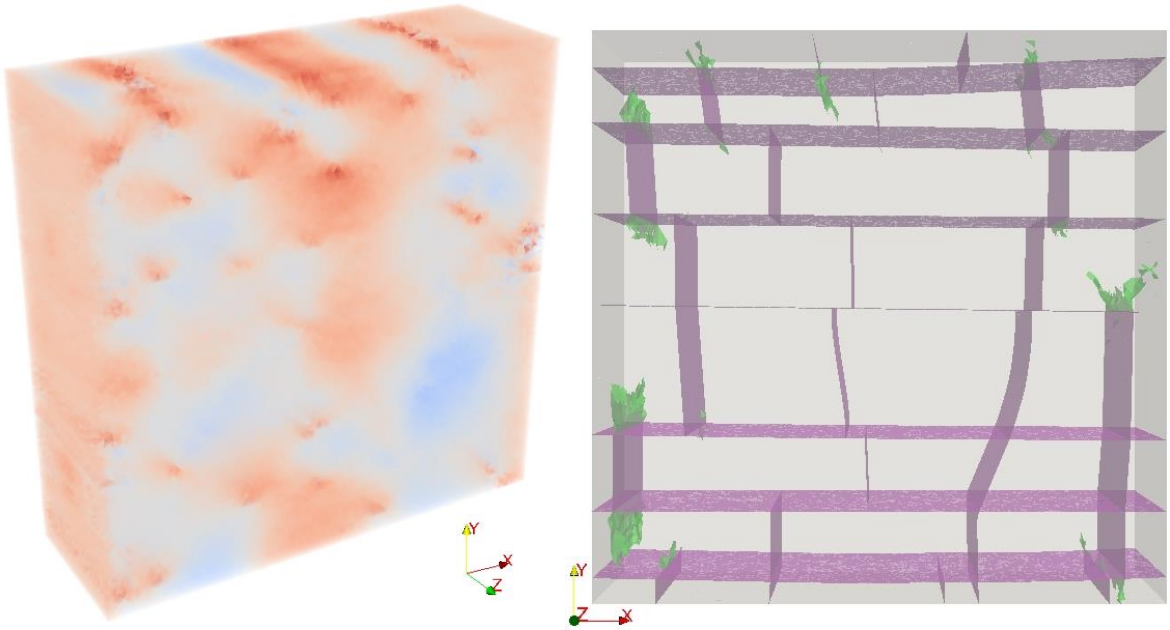

f. 3000 time-steps.

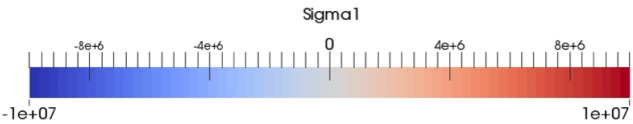

Figure 17: Stress and fracture evolution in the three-dimensional multi-layer model under an *in situ* stress condition. The figures on the left-hand side show colour contours of the magnitude of the maximum principal stress σ_1 ($\sigma_1 \geq \sigma_2 \geq \sigma_3$). The figures on the right-hand side show fracture development inside the model. Note that a semi-transparent colour scheme is used to differentiate discrete surfaces, where the grey colour represents model outer

boundaries; the purple colour represents original fracture sets; and the green colour represents newly developed fracture surfaces.

4 Discussion

The computational model described in this paper works on fixed meshes, which means it only allows fractures to propagate along tetrahedral element boundaries. This mesh dependency of fracture patterns is not significant if the element size is small enough compared with the scale of the domain (Guo et al., 2016). For example, in the Brazilian tests (Figure 8) although the fracture surfaces are not straight vertical planes, their roughness only deviates from the vertical direction by a small extent. Moreover, this mesh dependency provides convenience to realistically simulate fracturing behaviour along grain boundaries for some quasi-brittle low porosity igneous or sedimentary rocks, like granite and tight sandstone. It requires that the size of tetrahedral elements be of the same order of magnitude as the grain size. This condition can be satisfied for laboratory specimens, which can be meshed with a reasonable number of elements. Even when this condition is difficult to satisfy for large-scale engineering problems, which typically have scales of several orders of magnitude higher than the grain sizes of materials, acceptable macroscopic fracture patterns can still be obtained using large elements if their sizes are considerably smaller than the scale of the simulated domain.

The fracture model described in this paper has the ability of simulating both fracture initiation from intact material and fracture growth from single or multiple fracture tips. The materials in the numerical examples of this paper are all assumed to be homogeneous and isotropic. This assumption is a simplification of real material properties, and all the imperfections, e.g. flaws, impurities, etc., are neglected. In physical experiments, this assumption is valid when the microstructures that cause heterogeneity are negligible in isotropic materials, which usually happens when the scales of microstructures are considerably smaller than the scale of the whole model. In this case, failure in the model usually starts from the highest stress concentration zones. For example, in the Brazilian test tensile stresses progressively approach the strength limit near the centre, so the tensile

splitting fracture develops along the loading diametral direction. In these kinds of heterogeneous stress fields, homogeneous and isotropic material can give ideal results because the locations of fracturing are controlled by the stress distributions. However, for a loading geometry that is supposed to generate homogeneous stress fields, such as direct tension tests and polyaxial compression tests, in physical experiments even if the material specimens can be justifiably considered as homogeneous and isotropic, fractures would still initiate from some pre-existing imperfections that exist in the model before loading starts. If these imperfections are not represented properly in the numerical model specimen, the location of the first numerically grown fracture can be governed by largely stochastic processes, which are mainly influenced by the peak amplitudes of stress waves in the model and numerical instabilities. Therefore, the homogeneous and isotropic assumption for the material is well suited (for un-laminated or un-foliated rock types) when the stress field before fracturing is heterogeneous, but that to model the response of a more homogeneous stress field it may be more appropriate to introduce pre-existing fractures or flaws, like the work of Mahabadi et al. (2014), who proposed a micromechanical approach for introducing the geometrical and material heterogeneity of geomaterials into two-dimensional models.

Developed in the context of the combined finite-discrete element method, the computational model presented in this paper has the advantage of modelling tensile and shear fractures in complex stress domains. However, several limitations still exist. For example, a complete loading-unloading path is missing in the current model. After fracture formation, if unloading happens, the contact force (e.g. friction) between discrete fracture surfaces will be calculated by the DEM method; however, permanent fractures remain in the domain even when the external loading returns to zero. If the failed joint elements can be reconstructed, which means detached tetrahedral elements can be reconnected, it would greatly expand the area that this computational model can be applied, such as bone healing problems in the field of biomedical engineering. Another limitation is that the computational time can become unaffordable if the number of elements is significantly large, which is a common issue for fixed-mesh-based numerical models in serial codes. The small time-steps used in the simulations are mainly determined by the stability requirement. In the future, it is worth

exploring different numerical methods to ease the requirements on time-steps. In order to boost the simulation speed, one possible solution is parallel computing (Owen and Feng, 2001; Frantík et al., 2013; Shterenlikht et al, 2018). Another possible solution is the multiscale method, which can reduce computational cost for large-scale problems (Beex et al., 2014). Some examples of using different algorithms for the local domain around fractures include the SGBEM-FEM alternating method (Han and Atluri, 2002) and the substructuring FE-XFEM method (Wyart et al., 2008). These methods can expedite the simulation of large-scale problems and maintain the same accuracy. Similar approaches can be developed for the FEMDEM method, in which the fracture model is only applied to the subdomain around existing fractures and stress concentration zones.

5 Conclusions

A computational model has been developed using the combined finite-discrete element method (FEMDEM). The finite element formulation and the discrete element formulation are combined both in the space domain and in the time domain. In the space domain, the finite element formulation is used for the continuum (no fractures), while the discrete element formulation is used for the interaction across discontinuities, including multi-body interaction and normal compression and sliding friction between fracture surfaces. In the time domain, the continuity between tetrahedral elements is constrained by joint elements before fracture formation, then after fracture formation, the interaction between separated tetrahedral elements on both sides of the fracture is simulated by contact algorithms.

Brazilian tests and polyaxial compression tests were conducted to validate the computational model to simulate both tensile and shale failures. The Brazilian tests simulated the dynamic effect of different loading rates on the indirect tensile strength of the material. The polyaxial compression tests modelled the shear fracturing behaviour in compressive stress fields, such as shear directions and conjugate shearing, from different material properties. One multi-layer rock model extracted from a realistic fracture pattern was simulated in a true three-dimensional *in situ* stress condition as an example of applying the

computational model in engineering problems. The distribution of existing fractures had a significant effect on the formation of the fracture pattern because new fractures grew from stress concentrations caused by existing fractures. Three-dimensional stress heterogeneity caused by fracturing was accurately captured in this example.

The proposed three-dimensional fracture model is capable of simulating the entire fracturing process, including pre-peak hardening deformation, post-peak strain softening, transition from continuum to discontinuum, and the explicit interaction between discrete fracture surfaces for both tensile and shear fracture initiation and propagation. The numerical results show that the fracture model is able to generate fracture patterns according to mechanical principles of material failure. Both tensile and shear fractures can either initiate from stress concentrations in an intact domain or grow from existing fracture tips in complicated stress regimes. The computational model has been implemented into an in-house numerical code written in C and C++, and will later be released as open source so researchers have full flexibility to further develop the model for their customised use. It provides an ideal tool to examine in detail the three-dimensional fracture and fragmentation problems in quasi-brittle materials.

Acknowledgements

We are grateful for the support from Janet Watson scholarship provided by the Department of Earth Science and Engineering, Imperial College London for the first author's PhD project. The research has greatly benefited from projects that were running in parallel with this PhD study, notably the Gigantic Granular Systems project (EPSRC grant EP/H030123/1) and the itf-ISF oil company consortium on fractured reservoirs.

References

Andrade, J. E., Avila, C. F., Hall, S. A., Lenoir, N., and Viggiani, G. (2011). Multiscale modelling and characterization of granular matter: From grain kinematics to continuum mechanics. *Journal of the Mechanics and Physics of Solids*, 59:237-250.

Arthur, J. R. F., Dunstan, T., Al-Ani, Q. A. J. L., and Assadi, A. (1977). Plastic deformation and failure in granular media. *Géotechnique*, 27(1):53-74.

Atkinson, B. K. (1987). *Fracture mechanics of rock.* Academic Press.

Baraldi, D., Cecchi, A., and Tralli, A. (2015). Continuous and discrete models for masonry like material: A critical comparative study. *European Journal of Mechanics - A/Solids*, 50:39-58.

Beex, L.A.A., Peerlings, R.H.J., and Geers, M.G.D. (2014). A multiscale quasicontinuum method for dissipative lattice models and discrete networks. *Journal of the Mechanics and Physics of Solids*, 64:154-169.

Belayneh, M. and Cosgrove, J. W. (2004). Fracture-pattern variations around a major fold and their implications regarding fracture prediction using limited data: an example from the Bristol Channel Basin. *Geological Society, London, Special Publications 2004*, 231:89-102.

Belytschko, T. and Black, T. (1999). Elastic crack growth in finite elements with minimal remeshing. *International Journal for Numerical Methods in Engineering*, 45:601-620.

Bonet, J., Wood, R. D., 1997. *Nonlinear Continuum Mechanics for Finite Element Analysis*. Cambridge: Cambridge University Press, first edition.

Calvetti, F. (2008). Discrete modelling of granular materials and geotechnical problems. *European Journal of Environmental and Civil Engineering*, 12(7-8):951-965.

Chu, J. and Leong, W. K. (2002). Effect of fines on instability behaviour of loose sand. *Géotechnique*, 52(10):751-755.

Ciantia, M. O., Arroyo, M., Calvetti, F., and Gens, A. (2015). An approach to enhance efficiency of DEM modelling of soils with crushable grains. *Géotechnique*, 65(2):91-110.

Ciantia, M. O., Arroyo, M., Calvetti, F., and Gens, A. (2016). A numerical investigation of the incremental behavior of crushable granular soils. *International Journal for Numerical and Analytical Methods in Geomechanics*, 40:1773-1798.

Cil, M. B., Sohn, C., and Buscarnera, G. (2020). DEM modeling of grain size effect in brittle granular soils. *Journal of Engineering Mechanics*, 146(3):04019138.

Cundall, P. A. (2001). A discontinuous future for numerical modelling in geomechanics? *Proceedings of the Institute of Civil Engineers Geotechnical Engineering*, 149:41-47.

Cundall, P. A. and Strack, O. D. L. (1979). The development of constitutive laws for soils using distinct element method. In *Proceedings of the 3rd Numerical Methods in Geomechanics*, Aachen, Germany.

Daouadji, A., AlGali, H., Darve, F., and Zeghloul, A. (2010). Instability in granular materials: experimental evidence of diffuse mode of failure for loose sands. *Journal of Engineering Mechanics*, 136(5):575-588.

Darve, F., Servant, G., Laouafa, F., and Khoa, H. D. V. (2004). Failure in geomaterials: continuous and discrete analyses. *Computer Methods in Applied Mechanics and Engineering*, 193:3057-3085.

Delennen, J.-Y., El Youssoufi, M. S., Cherblanc, F., and Bénet, J.-C. (2004). Mechanical behaviour and failure of cohesive granular materials. *International Journal for Numerical and Analytical Methods in Geomechanics*, 28:1577-1594.

di Prisco, C. and Imposimato, S. (1997). Experimental analysis and theoretical interpretation of triaxial load controlled loose sand specimen collapses. *Mechanics of Cohesive-Frictional Materials*, 2:93-120.

Elmekati, A. and El Shamy, U. (2010). A practical co-simulation approach for multiscale analysis of geotechnical systems. *Computers and Geotechnics*, 37:494-503.

Engelder, T. and Peacock, D. C. (2001). Joint development normal to regional compression during flexural-flow folding: the Lilstock Buttress Anticline, Somerset, England. *Journal of Structural Geology*, 23:259-277.

Fairhurst, C. (1964). On the validity of the 'Brazilian' test for brittle material. *International Journal of Rock Mechanics & Mining Sciences*, 1:535-546.

François, B. and Keita, O. (2015). A microstructurally-based internal length for strain localization problems in dynamics. *European Journal of Mechanics - A/Solids*, 53:282-293.

Frantík, P., Veselý, V., and Keršner, Z. (2013). Parallelization of lattice modelling for estimation of fracture process zone extent in cementitious composites. *Advances in Engineering Software*, 60-61:48-57.

Griffith, A. A. (1921). The phenomena of rupture and flow in solids. *Philosophical Transactions of the Royal Society of London. Series A, Containing Papers of a Mathematical or Physical Character*, 221:163-198.

Gui, Y. L., Hu, W., Zhao, Z. Y., and Zhu, X. (2018). Numerical modelling of a field soil desiccation test using a cohesive fracture model with Voronoi tessellations. *Acta Geotechnica*, 13:87-102.

Guo, H., Aziz, N. I., and Schmidt, L. C. (1993). Rock fracture-toughness determination by the Brazilian test. *Engineering Geology*, 33:177-188.

Guo, L., Latham, J.-P., and Xiang, J. (2015). Numerical simulation of breakages of concrete armour units using a three-dimensional fracture model in the context of the combined finite-discrete element method. *Computers & Structures*, 146:117-142.

Guo, L., Latham, J.-P., and Xiang, J. (2017). A numerical study of fracture spacing and through-going fracture formation in layered rocks. *International Journal of Solids and Structures*, 110-111:44-57.

Guo, L., Xiang, J., Latham, J.-P., and Izzuddin, B. (2016). A numerical investigation of mesh sensitivity for a new three-dimensional fracture model within the combined finite-discrete element method. *Engineering Fracture Mechanics*, 151:70-91.

Guo, N. and Zhao, J. (2016a). 3D multiscale modeling of strain localization in granular media. *Computers and Geotechnics*, 80:360-372.

Guo, N. and Zhao, J. (2016b). Multiscale insights into classical geomechanics problems. *International Journal for Numerical and Analytical Methods in Geomechanics*, 40:367-390.

Hammer, P. C., Marlowe, O. J., and Stroud, A. H. (1956). Numerical integration over simplexes and cones. *Mathematics of Computation*, 10:130-137.

Han, Z. D. and Atluri, S. N. (2002). SGBEM (for cracked local subdomain) – FEM (for uncracked global structure) alternating method for analyzing 3D surface cracks and their fatigue-growth. *Computer Modeling in Engineering & Sciences*, 3(6):699-716.

Hillerborg, A., Modéer, M, and Petersson, P.-E. (1976). Analysis of crack formation and crack growth in concrete by means of fracture mechanics and finite elements. *Cement and Concrete Research*, 6: 773-782.

Huang, W., Sun, D., and Sloan, S. W. (2007). Analysis of the failure mode and softening behaviour of sands in true triaxial tests. *International Journal of Solids and Structures*, 44:1423-1437.

Jansari, C., Natarajan, S., Beex, L., and Kannan, K. (2019). Adaptive smoothed stable extended finite element method for weak discontinuities for finite elasticity. *European Journal of Mechanics - A/Solids*, 78:103824.

Kaneko, K. Terada, K., Kyoya, T., and Kishino, Y. (2003). Global-local analysis of granular media in quasi-static equilibrium. *International Journal of Solids and Structures*, 40:4043-4069.

Kh., A. Bagherzadeh, Mirghasemi, A. A., and Mohammadi, S. (2008). Micromechanics of breakage in sharp-edge particles using combined DEM and FEM. *Particuology*, 6:347-361.

Kh., A. Bagherzadeh, Mirghasemi, A. A., and Mohammadi, S. (2011). Numerical simulation of particle breakage of angular particles using combined DEM and FEM. *Powder Technology*, 205:15-29.

Khoa, H. D. V. , Georgopoulos, I. O., Darve, F., and Laouafa, F. (2006). Diffuse failure in geomaterials: Experiments and modelling. *Computers and Geotechnics*, 33:1-14.

Knappett, J. A. and Craig, R. F. (2012). *Craig's Soil Mechanics*. Spon Press, eighth edition.

Klein, P. A., Foulk, J. W., Chen, E. P., Wimmer, S. A., and Gao, H. J. (2001). Physics-based modeling of brittle fracture: cohesive formulations and the application of meshfree methods. *Theoretical and Applied Fracture Mechanics*, 37:99-166.

Klerck, P. A., Sellers, E. J., and Owen, D. R. J. (2004). Discrete fracture in quasi-brittle materials under compressive and tensile stress states. *Computer methods in applied mechanics and engineering*, 193:3035-3056.

Lade, P. V. (2002). Instability, shear banding, and failure in granular materials. *International Journal of Solids and Structures*, 39:3337-3357.

Lade P. V. and Wang, Q. (2001). Analysis of shear banding in true triaxial tests on sand. *Journal of Engineering Mechanics*, 127(8):762-768.

Lama, R. D. and Vutukuri, V. S. (1978). *Handbook on mechanical properties of rocks: testing techniques and results*. Trans Tech Publications.

Latham, J.-P., Munjiza, A., Mindel, J., Xiang, J., Guises, R., Garcia, X., … Piggott, M. (2008). Modelling of massive particulates for breakwater engineering using coupled FEMDEM and CFD. *Particuology*, 6:572-583.

Li, X., Liang, Y., Duan, Q., Schrefler, B. A., and Du, Y. (2014). A mixed finite element procedure of gradient Cosserat continuum for second-order computational homogenisation of granular materials. *Computational Mechanics*, 54:1331-1356.

Li, X., Chu, X, and Feng, Y. T. (2005). A discrete particle model and numerical modeling of the failure modes of granular materials. *Engineering Computations*, 22(8):894-920.

Lobo-Guerrero, S. and Vallejo, L. E. (2005). Discrete element method evaluation of granular crushing under direct shear test conditions. *Journal of Geotechnical and Geoenvironmental Engineering*, 131(10):1295-1300.

Lockner, D. A., Byerlee, J. D., Kuksenko, V., Ponomarev, A., and Sidorin, A. (1991). Quasi-static fault growth and shear fracture energy in granite. *Nature*, 350:39-42.

Ma, G., Zhou, W., Chang, X.-L., and Chen, M.-X. (2016). A hybrid approach for modeling of breakable granular materials using combined finite-discrete element method. *Granular Matter*, 18:7.

Ma, G., Chen, Y., Yao, F., Zhou, W., and Wang, Q. (2019). Evolution of particle size and shape towards a steady state: Insights from FDEM simulations of crushable granular materials. *Computers and Geotechnics*, 112:147-158.

Mahabadi, O. K., Lisjak, A., Grasselli, G., Lukas, T., and Munjiza, A. (2010). Numerical modelling of a triaxial test of homogeneous rocks using the combined finite-discrete element method. In *Proceedings of the ISRM International Symposium – EUROCK 2010*, Lausanne, Switzerland.

Mahabadi, O. K., Lisjak, A., Munjiza, A., and Grasselli, G. (2012). Y-Geo: new combined finite-discrete element numerical code for geomechanical applications. *International Journal of Geomechanics*, 12:676-688.

Mahabadi, O. K., Randall, N. X., Zong, Z., and Grasselli, G. (2012). A novel approach for micro-scale characterization and modelling of geomaterials incorporating actual material heterogeneity. *Geophysical Research Letters*, 39:L01303.

Mahabadi, O. K., Tatone, B. S. A., and Grasselli, G. (2014). Influence of microscale heterogeneity and microstructure on the tensile behaviour of crystalline rocks. *Journal of Geophysical Research: Solid Earth*, 119:5324-5341.

Malekan, M., Silva, L. L., Barros, F. B., Pitangueira, R. L.S., and Penna, S. S. (2018). Two-dimensional fracture modeling with the generalized/extended finite element method: An object-oriented programming approach. *Advances in Engineering Software*, 115:168-193.

Martin, C. L., Bouvard, D., and Shima, S. (2003). Study of particle rearrangement during powder compaction by the Discrete Element Method. *Journal of the Mechanics and Physics of Solids*, 51:667-693.

Meng, F. and Thouless, M.D. (2019). Cohesive-zone analyses with stochastic effects, illustrated by an example of kinetic crack growth. *Journal of the Mechanics and Physics of Solids*, 132:103686.

Miehe, C., Dettmar, J., and Zäh, D. (2010). Homogenization and two-scale simulations of granular materials for different microstructural constraints. *International Journal for Numerical Methods in Engineering*, 83:1206-1236.

Monteiro Azevedo, N. and Lemos, J. V. (2006). Hybrid discrete element/finite element method for fracture analysis. *Computer Methods in Applied Mechanics and Engineering*, 195:4579-4593.

Morris, J. P., Rubin, M. B., Blair, S. C., Glenn, L. A., and Heuze, F. E. (2004). Simulations of underground structures subjected to dynamic loading using the distinct element method. *Engineering Computations*, 21:384-408.

Morris, J. P., Rubin, M. B., Block, G. I., and Bonner, M. P. (2006). Simulations of fracture and fragmentation of geologic materials using combined FEM/DEM analysis. *International Journal of Impact Engineering*, 33:463-473.

Munjiza, A. (2004). *The combined finite-discrete element method*. New York: Wiley and Sons, first edition.

Munjiza, A. and Andrews, K. R. F. (1998). NBS contact detection algorithm for bodies of similar size. *International Journal for Numerical Methods in Engineering*, 43:131-149.

Munjiza, A. and Andrews, K. R. F. (2000). Penalty function method for combined finite-discrete element systems comprising large number of separate bodies. *International Journal for Numerical Methods in Engineering*, 49:1377-1396.

Munjiza, A., Andrews, K. R., and White, J. K. (1999). Combined single and smeared crack model in combined finite-discrete element analysis. *International Journal for Numerical Methods in Engineering*, 44:41-57.

Nadimi, S. and Fonseca, J. (2018). A micro finite-element model for soil behaviour. *Géotechnique*, 68(4):290-302.

Nelson, R. A. (2001). *Geological analysis of naturally fractured reservoirs*. Houston: Gulf Professional Publishing, second edition.

Nguyen, T. K., Combe, G., Caillerie, D., and Desrues, J. (2014). FEM×DEM modelling of cohesive granular materials: numerical homogenisation and multi-scale simulations. *Acta Geophysica*, 62(5):1109-1126.

Nicot, F., Sibille, L., Donze, F., and Darve, F. (2007). From microscopic to macroscopic second-order work in granular assemblies. *Mechanics of Materials*, 39:664-684.

Nicot, F., Daouadji, A., Laouafa, F., and Darve, F. (2011). Second-order work, kinetic energy and diffuse failure in granular materials. *Granular Matter*, 13:19-28.

Obermayr, M., Dressler, K., Vrettos, C., and Eberhard, P. (2013). A bonded-particle model for cemented sand. *Computers and Geotechnics*, 49:299-313.

Oliver, J. (1996). Modelling strong discontinuities is solid mechanics via strain softening constitutive equations. Part 1: fundamentals. *International Journal for Numerical Methods in Engineering*, 39:3575-3600.

Oñate, E. and Rojek, J. (2004). Combination of discrete element and finite element methods for dynamic analysis of geomechanics problems. *Computer Methods in Applied Mechanics and Engineering*, 193:3087-3128.

Ord, A. and Hobbs, B. E. (2010). Fracture pattern formation in frictional, cohesive, granular material. *Philosophical Transactions of the Royal Society A*, 368:95-118.

Ortiz, M., Leroy, Y., and Needleman A. (1987). A finite element method for localised failure analysis. *Computer Methods in Applied Mechanics and Engineering*, 61:189-214.

Owen, D. R. J. and Feng, Y. T. (2001). Parallelised finite/discrete element simulation of multi-fracturing solids and discrete systems. *Engineering Computations*, 18:557-576.

Paavilainen, J., Tuhkuri, J., and Polojärvi, A. (2009). 2D combined finite-discrete element method to model multi-fracture of beam structures. *Engineering Computations*, 26(6):578-598.

Peron, H., Delenne, J. Y., Laloui, L., and El Youssoufi, M. S. (2009). Discrete element modelling of drying shrinkage and cracking of soils. *Computers and Geotechnics*, 36:61-69.

Popovics, S. (1998). *Strength and related properties of concrete: a quantitative approach*. John Wiley & Sons.

Price, N. J. and Cosgrove, J. W. (1990). *Analysis of geological structures.* Cambridge: Cambridge University Press, first edition.

Radi, K., Jauffrès, D., Deville, S., and Martin, C. L. (2019). Elasticity and fracture of brick and mortar materials using discrete element simulations. *Journal of the Mechanics and Physics of Solids*, 126:101-116.

Rougier, E., Knight, E. E., Broome, S. T., Sussman, A. J., and Munjiza, A. (2014). Validation of a three-dimensional finite-discrete element method using experimental results of the Split Hopkinson Pressure Bar test. *International Journal of Rock Mechanics & Mining Sciences*, 70:101-108.

Salehani, M. K., Irani, N., and Nicola, L. (2019). Modeling adhesive contacts under mixed-mode loading. *Journal of the Mechanics and Physics of Solids*, 130:320-329.

Schellekens, J. C. J. and de Borst, R. (1993). A non-linear finite element approach for the analysis of mode-I free edge delamination in composites. *International Journal of Solids and Structures*, 30(9):1239-1253.

Shi, G. and Goodman, R. E. (1985). Two dimensional discontinuous deformation analysis. *International Journal for Numerical and Analytical Methods in Geomechanics*, 9(6):541-556.

Shterenlikht, A., Margetts, L., and Cebamanos, L. (2018). Modelling fracture in heterogeneous materials on HPC systems using a hybrid MPI/Fortran coarray multi-scale CAFE framework. *Advances in Engineering Software*, 125:155-166.

Sibille, L., Nicot, F., Donzé, F. V., and Darve, F. (2007). Material instability in granular assemblies from fundamentally different models. *International Journal for Numerical and Analytical Methods in Geomechanics*, 31:457-481.

Sibille, L., Donzé, F.-V., Nicot, F., Chareyre, B., and Darve, F. (2008). From bifurcation to failure in a granular material: a DEM analysis. *Acta Geotechnica*, 3:15-24.

Tu, F., Ling, D., Hu, C., and Zhang, R. (2017). DEM-FEM analysis of soil failure process via the separate edge coupling method. *International Journal for Numerical and Analytical Methods in Geomechanics*, 41:1157-1181.

Turon, A., Dávila, C. G., Camanho, P. P, and Costa, J. (2007). An engineering solution for mesh size effects in the simulation of delamination using cohesive zone models. *Engineering Fracture Mechanics*, 74:1665-1682.

Tvergaard, V. (2003). Cohesive zone representations of failure between elastic or rigid solids and ductile solids. *Engineering Fracture Mechanics*, 70:1859-1868.

Tvergaard, V. (2015). Study of localization in a void-sheet under stress states near pure shear. *International Journal of Solids and Structures*, 75-76:134-142.

Vardoulakis, I. (1980). Shear band inclination and shear modulus of sand in biaxial tests. *International Journal for numerical and analytical methods in geomechanics*, 4:103-119.

Vermeer, P. A. (1990). The orientation of shear bands in biaxial tests. *Géotechnique*, 40(2):223-236.

Vermeer, P. A. and de Borst, R. (1984). Non-associated plasticity for soils, concrete and rock. *Heron*, 29(3):3-64.

Wang, Q. and Lade, P. V. (2001). Shear banding in true triaxial tests and its effect on failure in sand. *Journal of Engineering Mechanics*, 127(8):754-761.

Wang, J. and Yan, H. (2013). On the role of particle breakage in the shear failure behavior of granular soils by DEM. *International Journal for Numerical and Analytical Methods in Geomechanics*, 37:832-854.

Wu, H. and Pollard, D. D. (1995). An experimental study of the relationship between joint spacing and layer thickness. *Journal of Structural Geology*, 17(6):887-905.

Wyart, E., Duflot, M., Coulon, D., Martiny, P., Pardoen, T., Remacle, J.-F., and Lani, F. (2008). Substructuring FE-XFE approaches applied to three-dimensional crack propagation. *Journal of Computational and Applied Mathematics*, 215:626-638.

Xian, L., Bicanic, N., Owen, D. R. J., and Munjiza, A. (1991). Rock blasting simulation by rigid body dynamics analysis and rigid brittle fracturing model. In Bicanic, N. et al., editors, *Proceedings NEC-91, International Conference on Nonlinear Engineering Computations*, 577-587, Pineridge Press, Swansea, UK.

Xiang, J., Munjiza, A., and Latham, J.-P. (2009). Finite strain, finite rotation quadratic tetrahedral element for the combined finite-discrete element method. *International Journal for Numerical Methods in Engineering*, 79:946-978.

Yan, B., Regueiro, R. A., and Sture, S. (2010). Three-dimensional ellipsoidal discrete element modelling of granular materials and its coupling with finite element facets. *Engineering Computations*, 27(4):519-550.

Zhao, J. and Guo, N. (2015). The interplay between anisotropy and strain localisation in granular soils: a multiscale insight. *Géotechnique*, 65(8):642-656.

Zoback, M. D. (2010). *Reservoir geomechanics*. New York: Cambridge University Press.